Mon. Not. R. astr. Soc. (1985) **215,** 1–36

Detailed observations of NGC 4151 with *IUE* – IV. Absorption line spectrum and variability*

G. E. Bromage,[1] A. Boksenberg,[2] J. Clavel,[3] A. Elvius,[4] M. V. Penston,[2] G. C. Perola,[5] M. Pettini,[2] M. A. J. Snijders,[2] E. G. Tanzi[6] and M. H. Ulrich[7]

[1] *Astrophysics Group, Rutherford Appleton Laboratory, Chilton, Didcot, Oxfordshire OX11 0QX*

[2] *Royal Greenwich Observatory, Herstmonceux Castle, Hailsham, East Sussex BN27 1RP*

[3] *Observatoire de Meudon, 92190 Meudon, France*

[4] *Stockholm Observatory, 13300 Saltsjobaden, Sweden*

[5] *Istituto Astronomico, Università di Roma, Via Lancisi 29, 00161 Roma, Italy*

[6] *Istituto de Fisica Cosmica, CNR, 20133 Milano, Italy*

[7] *European Southern Observatory, 8046 Garching bei München, Germany*

Accepted 1984 December 7. Received 1984 December 4; in original form 1983 November 15

Summary. A detailed analysis is presented of the ultraviolet ($\lambda\lambda$ 1150–3200 Å) absorption spectrum of the NGC 4151 Seyfert nucleus. The *IUE* data base consisted of high-dispersion ($\Delta\lambda \sim 0.2$ Å) spectra at 5 epochs, and 137 low-dispersion ($\Delta\lambda \sim 4$–8 Å) spectra at 31 epochs from 1978 February to 1980 May, together with further low-dispersion data in 1980–81 with NGC 4151 in a very faint quiescent state.

Over 30 UV absorption lines are identified, including resonance and excited fine-structure lines, and absorptions from higher metastable levels. There is a strong unidentified blend at λ 1364/1370 Å. Correlation analyses are presented for 16 strong features in the mean low-dispersion spectra for 31 epochs. This coverage includes a large flare in 1979 May. For the highly ionized species (notably N v), equivalent widths (W_λ) are correlated with the non-thermal continuum flux. Several low-ion absorptions are perfectly correlated in W_λ

*Based on observations with the *International Ultraviolet Explorer* collected principally at the European Space Agency's Villafranca Satellite Tracking Station.

amongst themselves; in general they show moderately strong *anti*-correlations with continuum flux. All absorption lines appear to be weak when the nucleus is very faint.

Velocity ranges covered by absorptions are typically -1100 to $+100\,\mathrm{km\,s^{-1}}$ relative to the narrow emission lines, and show no obvious dependence on line excitation. Between faint and bright phases the lines of highly ionized species become slightly less negative in velocity but do not change dramatically in overall profile. Observed line widths at high dispersion, together with a detailed study of Si IV doublet ratios, yield an approximately constant effective b value of $\sim 500\,\mathrm{km\,s^{-1}}$, that is, a constant spread in velocity of the 'assemblage of clouds' in the absorption region. Thus the absorption-line variations are due largely to changes in the column density (N) of the species absorbing, rather than to changes in the velocity-spread (b value) of the clouds. Our observations suggest a model for the BLR absorption region consisting of large numbers of clouds that are almost optically thin – at variance with the Ferland & Mushotzky models.

A lower limit on the total H column density is obtained from those Si and C lines observable in the new UV spectra: $N(\mathrm{H}) \gtrsim 10^{21}\,\mathrm{cm^{-2}}$, consistent with observed X-ray absorptions. The population of C III and Si III *ns np* ^3P metastable absorbers is considerable: the present data imply $N(\mathrm{C\,III}, {}^3P)/N(\mathrm{C\,IV}, g)$ exceeds 10^{-2}, too high for recombination-dominated population. This result together with observed recombination times and other considerations, points to electron densities in the range $10^{8.5}$ to $10^{10}\,\mathrm{cm^{-3}}$.

Considering the likely space densities, the observed range of emission velocities covered, and the lack of any clear time lags in the absorbers' response to continuum flares, the most likely site of absorption is in a shell in the outermost parts of the BLR. Such a shell would have a thickness much less than 1 per cent of its distance from the centre; the mass of the absorption region would be roughly of order $1\,M_\odot$; and the mass loss rate from the NGC 4151 nucleus (if the loss were episodic rather than continuous) would only be about $10^{-2}\,M_\odot\,\mathrm{yr^{-1}}$.

1 Introduction

The ultraviolet spectrum of the brightest Type 1 Seyfert NGC 4151 nucleus has been monitored with the *International Ultraviolet Explorer* (*IUE*) since 1978 February. The rich absorption line spectrum is investigated in this paper. Earlier absorption studies (Anderson 1974 and earlier references therein; Davidsen & Hartig 1978; Boksenberg *et al.* 1978; Penston *et al.* 1979; Penston *et al.* 1981 – Paper I in the present series) have demonstrated the importance of the absorption spectrum for modelling of the nuclear layers of NGC 4151.

The presence in NGC 4151 of a large column density of hydrogen producing soft X-ray absorption (Ives, Sanford & Penston 1976; Barr *et al.* 1977) suggested there should be many strong lines in the UV spectrum. A discussion of some of these absorption lines was given in Paper I (Penston *et al.* 1981) in relation to seven epochs of low-dispersion observation in the first year of *IUE* operations.

The general location of the species responsible for the absorption spectra has been discussed briefly in Paper I. The strength and variability of many of the lines (including some from metastable lower levels) suggests that most of the absorbers are situated in the active nucleus of NGC 4151, rather than in the general interstellar medium of our Galaxy or of the NGC 4151 galaxy.

The present paper greatly extends the absorption analysis to cover 47 epochs between 1978

February and 1981 July. The main *IUE* low-dispersion analysis refers to 31 epochs with spacings of 0.5 day to 2 months between 1978 February and 1980 May. For this monitoring period, the UV, X-ray and visible continuum changes have been described and analysed by Perola *et al.* (1982 – Paper II); and the strong emission lines' variability, by Ulrich *et al.* (1984 – Paper III).

The present paper (IV) also includes an analysis of *IUE high*-dispersion spectra at 5 epochs in 1978–79, and of some absorption lines at 11 epochs in 1980–81 when the nucleus was very faint (including detailed monitoring in 1981 April–July). The nucleus apparently remained in this quiescent, very faint state from 1981 April (or earlier) until 1982 July (Gill *et al.* 1984).

A brief summary of some of the results presented here was given by Bromage *et al.* (1982) in conference proceedings. Full details of the *IUE* monitoring observations and an atlas of low-dispersion spectra will be given in a later paper in this series (Snijders *et al.* 1985, in preparation – Paper VI).

The present paper is arranged as follows. The observational data are summarized in Section 2. The measurements of equivalent widths and velocities from these *IUE* spectra are described in Section 3. Sections 4, 5 and 6 then give results and discussion of particular aspects of the analysis: on the equivalent widths and velocity variations and their correlations with continuum flux (Section 4); on the derivation of column densities in the absorption region of NGC 4151 (Section 5); and on the estimation of electron densities in the absorption region (Section 6). Finally, in a general discussion section (Section 7) we draw together the main conclusions and discuss their implications for models of the absorption line region – its structure, density, ionization conditions, location and size.

2 Observational data

The *IUE* observations used for this paper are summarized in Table 1. Estimates of optical magnitudes for the nucleus, derived from the *IUE* Fine Error Sensor (FES) and approximately corrected for contamination by starlight from the NGC 4151 galaxy (see Paper II), are included in the table.

A total of 137 spectra at *low resolution* (4–8 Å) were taken with *IUE* between 1978 February and 1980 May. They are listed in Paper II (Perola *et al.* 1982), and have been reduced with a uniform procedure which is described in Papers I and II. Weighted mean spectra were derived for 31 epochs with separations of 0.5 day to 2 months. For most epochs both short-wave ($\lambda\lambda$ 1150–1950 Å) and long-wave ($\lambda\lambda$ 1900–3250 Å) regions were covered.

During this period, five important continuum changes on time-scales of the order of 5–30 days were seen (Paper II). Here these 'events' will be labelled I1, I2, I3, D1 and D2, signifying three increases and two decreases. Of particular importance for the absorption analysis is the large flare of 1979 May (Event I1).

Intensive monitoring was resumed in 1981 April-July. It can be seen from the FES data in Table 1 that the nucleus remained very faint during this 1981 period, fainter than ever previously seen with *IUE*. However, even in this low state, the nucleus was not truly quiescent: both optical magnitudes (Table 1) and ultraviolet continuum fluxes (Table 6c) varied, usually together. For example, there was a 'mini-flare' event in late June 1981. The lowest fluxes were recorded in 1981 May 08: the far-ultraviolet continuum was then 2.3 mag fainter than in 1978 April, when the UV fluxes were the highest so far recorded.

To complete the low-dispersion data set for 1978–81, three images taken by other observers in 1980 were retrieved from the *IUE* Data Bank. These are also noted in Table 1.

In addition to the low-dispersion database, the present paper discusses the five short-wave *high-dispersion* spectra of NGC 4151 (resolution ~0.2 Å) taken with *IUE* during the same period. These are also listed in Table 1. All were taken through the large aperture to maximize the rather

Table 1. Journal of observations of NGC4151 with *IUE* during 1978–81.

(All images listed here were obtained with the large aperture)

The quoted magnitude is the IUE Fine Error Sensor magnitude, corrected empirically for a contribution of $13^{m}.07$ from the surrounding galaxy (see Paper II).

EPOCH	IMAGE	EXP. TIME (mins)	m (FES-gal)
A. HIGH DISPERSION			
1978			
Aug 01.9	SWP 2170	300	12.52 ± .04
Oct 23.9	3114	433	12.57 ± .06
Dec 25.5	3704	400	12.90 ± .06
1979			
May 20.2	SWP 5310	435	12.52 ± .05
May 26.2	5364	426	12.52 ± .05
B. LOW DISPERSION			
1978 Feb 28.7 to 1979 Dec 14.0 and 1980 Jan 01.4 to May 19.3	137 spectra at 31 epochs: for full journal of observations see Table 1 of Perola *et al.* 1982 (Paper II) (total observed range in $m_{(FES-gal)} \simeq 12.4$-12.9)		
Jul 30.49	SWP 9627	15	(from Data Bank)
Nov 27.44	SWP 10682	3x35 pseudo-trailed	(from Data Bank)
27.49	LWR 9392	15	(from Data Bank)
1981			
Apr 26.32	SWP 13810	25	13.24 ± .03
26.35	LWR 10448	30	
26.37	SWP 13811	40	
26.40	LWR 10449	25	
Apr 30.28	SWP 13845	25	13.24 ± .03
30.31	LWR 10479	25	
30.34	SWP 13846	50	
30.37	LWR 10480	25	

Table 1 – *continued*

EPOCH	IMAGE	EXP. TIME (mins)	m (FES-gal)
May 04.04	SWP 13880	25	13.31 ± .03
04.06	LWR 10511	30	
04.09	SWP 13881	40	
04.12	LWR 10512	25	
04.15	SWP 13882	60	
May 08.05	LWR 10543	30	13.38 ± .04
08.11	SWP 13921	154	
May 12.12	LWR 10574	25	13.22 ± .03
12.15	SWP 13961	25	
12.17	LWR 10575	25	
12.20	SWP 13962	50	
May 17.05	SWP 13982	30	13.30 ± .04
17.07	LWR 10630	30	
17.12	SWP 13983	120	
May 23.12	LWR 10680	30	13.14 ± .03
23.14	SWP 14030	30	
23.18	LWR 10681	60	
23.24	SWP 14031	120	
May 25.24	LWR 10700	30	13.11 ± .04
25.27	SWP 14057	50	
25.31	LWR 10701	50	
May 30.03	SWP 14115	30	13.20 ± .04
30.06	LWR 10748	45	
30.12	SWP 14116	120	
Jun 05.13	SWP 14189	30	13.14 ± .04
05.16	LWR 10784	30	
05.21	SWP 14190	96	
Jun 08.96	SWP 14222	30	13.20 ± .03
08.98	LWR 10813	30	
09.04	SWP 14223	120	
09.10	LWR 10814	48	
Jun 26.01	SWP 14332	30	13.01 ± .05
Jun 27.95	SWP 14348	30	13.12 ± .05
Jun 29.95	SWP 14359	30	13.15 ± .04
29.98	LWR 10968	30	
Jul 03.88	SWP 14392	25	13.12 ± .04
03.91	LWR 11004	25	
Jul 06.88	SWP 14412	60	13.16 ± .04
06.91	LWR 11019	30	
Jul 16.86	SWP 14495	30	13.27 ± .03
16.89	LWR 11071	30	
16.94	SWP 14496	100	
16.99	LWR 11072	30	
Jul 27.89	SWP 14573	30	13.12 ± .05
Jul 29.90	LWR 11185	120	13.14 ± .05

weak signal. Some results from two of the spectra have already been reported by Penston *et al.* (1979). All data have now been reprocessed with the correct ITF (Holm 1979) using a special version of IUESIPS which removes strong noise spikes by filtering the raw images with a median filter, thus greatly improving signal-to-noise for very weak images such as these. The signal-to-noise was further enhanced by adding relevant individual high-dispersion spectra.

The nucleus was bright at all high-dispersion epochs except 1978 December 25 when it was in a low state (see the FES magnitudes listed in Table 1). The 1978 October 23 observation was during the decay event D1 and in fact indicates that most of the continuum decline occurred *after* October 23, with a very short two-folding time of $\lesssim$5 days (*cf.* Paper II, where the previous best estimate was $\lesssim$10 days for this event).

3 Line identifications and measurements

3.1 ABSORPTION LINE IDENTIFICATIONS

Sixteen strong absorption features have been studied in detail, using the high signal-to-noise (low-dispersion) spectra. These 16 features are listed in Table 2 with their adopted definitions for measurement purposes. In addition, many other lines were detected in the low-dispersion or the high-dispersion data, and Table 3 gives a complete line list. Many of the identifications are indicated in Figs 1 and 2.

In Fig. 1, sections from a mean high-dispersion spectrum are plotted. Fig. 2 shows extracts of typical low-dispersion spectra. They were chosen to represent a 'very low' state (1981 May 23 example), a 'low' state (1979 May 3) and 'high' states (1978 May and 1979 May 19) of the nuclear continuum flux (*cf.* Papers II and III).

It is clear that the NGC 4151 absorption spectrum is very rich in the ultraviolet. Resonance lines are now seen from H I, C II, C IV, N V, O I, Mg I, Mg II, Al II, Al III, Si II, Si III, Si IV, S II and Fe II. Excited ground-term (fine structure) lines of C II, O I, Si II and Fe II (up to 0.12 eV) are clearly present. Furthermore, higher metastable levels are populated too, including C III and Si III *ns np* ^3P (6.5 eV), H I n=2 (10.2 eV – Balmer lines), He I 1*s*2*s* ^3S (19.7 eV), and probably He II n=2 (40.6 eV) and Si II and Al II (~5 eV). Population mechanisms for these excited levels are discussed later in this paper.

There is only one important feature that has defied explanation – a strong unidentified blend of absorption lines at $\lambda\lambda$ 1364, 1370 Å (±2 Å). Its strength and behaviour points to a very common element and a low stage of ionization (*cf.* the behaviour of low ions like Si II in Fig. 2). However, it is difficult to understand the existence of such an omission from the multiplet tables. The alternative, of a transient high-velocity component of a different line (e.g. Si IV at $-6700\,\mathrm{km\,s^{-1}}$) is yet more unlikely, since the feature reappeared in the same place nearly a year later when the continuum fell again to a 'low' state, whilst no corresponding high-velocity components of other lines were ever seen. There are wavelength coincidences with the main resonance line of B II at λ 1362.46 and the excited O V 2*s*–2*p* ^1P–^1D line at λ 1371, but we are sceptical about these possibilities. The boron abundance would have to be a factor 10^4 higher than normal, whilst the relevant O V level is not metastable and a density exceeding $n_e \sim 10^{13}\,\mathrm{cm^{-3}}$ would be needed to see λ 1371 in absorption. (The isoelectronic C IIIλ 2296 line is never seen in absorption, only in emission – *cf.* Fig. 2.) Furthermore, the observed blend $\lambda\lambda$ 1364, 1370 behaves as if both components derive from a common (or similar) ion. The feature thus remains a mystery.

3.2 MEASUREMENTS FROM LOW-DISPERSION SPECTRA

The present set of weighted mean *low-dispersion* data have sufficiently high signal-to-noise ratios to enable equivalent widths and mean wavelengths to be accurately measured. The 16 features

Table 2. Definition of absorption features measured from the low-dispersion spectra.

REFERENCE WAVELENGTH λ_{lab}(Å) (1)	MAIN CONTRIBUTORS (2)	INTEGRATION REGION (wavelengths in Å) (3)	LOCAL CONTINUUM DEFINITION (wavelengths in Å) (4)
1175.70	CIII** (4)	1167-1182	mean of 1155-1167 & 1182-1187
1191.90	Si II,Si II*(5)	1187-1198	linear, between 1185 & 1200
1240.14	N V (1)	1234-1250 (Si weak) 1234-1245 (Si strong)	LLC: linear, between samples at ends of integration region
1260.42	Si II, Si II* (4)	1254-1275 (weak) 1249-1280 (strong)	linear, between 1246-54 & 1275-88 linear, between 1243-49 & 1280-88
1303.27	Si III** (4) Si II (3), OI (2)	1288-1313	mean of 1275-1288 & 1313-1325
1334.53	C II, C II* (1)	1326-1343	mean of 1313-1326 & 1343-1355
1368.00	Unidentified blend	1355-1378	mean of 1343-1355 (extrapolated)
1393.75	Si IV (1)	1384.5-1399.3	LLC: linear, between the apparent emission maxima
1402.77	Si IV (1)	1399.3-1411.3	HLC: fitted emission line profile centred on λ 1402 Å
1526.71	Si II, Si II* (2)	1520-1535	linear, between samples at ends of integration region
1549.10	C IV (1)	1541-1557	LLC: linear, between the apparent emission maxima
1608.46	Fe II (8)	1604-1614	linear, between 1598-1604 and 1614-1622
1857.41	Al III (1) Al II** (4)	1849-1875	mean of 1828-1849 (extrapolated)
2599.40	Fe II (1)	2591-2608	mean of 2536-2572 and 2612-2647
2797.92	Mg II (1)	2787-2809	LLC: linear, between the apparent emission maxima
2945.10	He I** (1)	2938-2954	mean of 2897-2938 and 2954-2994

(1) λ_{lab} is the wavelength of the resonance line in the feature (or, mean of unsaturated lines when more than one resonance line contributes) at zero redshift, and in vacuum for $\lambda < 2000$ Å. When no resonance lines are expected, the adopted λ_{lab} is an appropriate mean reference wavelength for zero redshift.

(2) UV multiplet numbers are given in brackets. Throughout this paper, the convention is adopted whereby x, x^* and x^{**} are absorptions from the ground level, excited fine structure levels and higher metastable levels, respectively.

(3) The extended integration region for Si II λ1260 applies to epochs 1979 May 3–4 and 1980 March 1–6 only.

(4) LLC=low, HLC=high local continuum. LLC give lower limits to equivalent widths. The Si IV case is discussed in Section 3.2.

(5) For the 'very low state' epochs, especially the 1981 data, the definitions of λ1240 and λ1260 had to be modified to avoid the narrower N V emission line. Indeed λ1240 absorption was usually not measurable for this reason. Similarly, weak C II λ1335 emission was avoided where necessary in measuring the λ1335 absorption.

Table 3. Absorption lines in NGC4151 spectra, λλ1170–3200 Å.

Multiplet(UV)		Transitions		λ(Å)	Measurements and Comments
C III**	4	$2s2p-2p^2$	$^3P-^3S$	1176 bl	measured: see Tables 4,5
Si II	5	$3s^23p-3s3p^2$	$^2P_{\frac{1}{2}}-^2P$	1190,1193	measured: see Tables 4,5
Si II*	5		$^2P_{\frac{3}{2}}-^2P$	1194,1197	measured: see Tables 4,5
Si III	2	$3s^2-3s3p$	$^1S-^1P$	1207	present
H I	1	1s-2p	$^2S-^2P$	1216	λ measured: see Table 7
N V	1	2s-2p	$^2S-^2P$	1239,1243	measured: see Tables 4,5,7
Si II**	8	$3s3p^2-3p^3$	$^4P-^4S$	1248,1251	possibly present
S II	1	$3s^23p^3-3s3p^4$	$^4S-^4P$	1251,1254, 1260	present (high dispersion)
Si II	4	$3s^23p-3s^23d$	$^2P_{\frac{1}{2}}-^2D$	1260	blend with S II, Fe II
Si II*	4		$^2P_{\frac{3}{2}}-^2D$	1265	measured: see Tables 4,5,7
Fe II	9	a - x	$^6D_{\frac{9}{2}}-^6P$	1261	blended, see above
Fe II*	9		$^6D_{\frac{7}{2}}-^6P$	1267	blended, see above
Fe II*	9		$^6D_{\frac{5}{2},\frac{3}{2}}-^6P$	1272,1276	probably present: see Figure 2
Si III**	4	$3s3p-3p^2$	$^3P-^3P$	1295-1303bl	present (high dispersion) and probably dominates blend
Si II	3	$3s^23p-3s3p^2$	$^2P_{\frac{1}{2}}-^2S$	1304	blend with O I, Si III**
Si II*	3		$^2P_{\frac{3}{2}}-^2S$	1309	measured: see Tables 4,5,7
O I	2	$2p^4-2p^33s$	$^3P_2-^3S$	1302	blended, see above
O I*	2		$^2P_{1,0}-^3S$	1305 bl	blended, see above
C II	1	$2s^22p-2s2p^2$	$^2P_{\frac{1}{2}}-^2D$	1335	measured: see Tables 4,5,7
C II*	1		$^2P_{\frac{3}{2}}-^2D$	1336	measured: see Tables 4,5,7
Si II**	7	$3s3p^2-3s3p4s$	$^4P-^4P$	1347-1354bl	probably present (Figure 2)

Table 3 – *continued*

Multiplet(UV)		Transitions		λ(A)	Measurements and Comments
(Unidentified)		?	?	1364,1371	blend measured: Tables 4,5
Si IV	1	3s-3p	$^2S-^2P_{\frac{3}{2}}$	1394	measured: see Tables 4,5,7
Si IV	1		$^2S-^2P_{\frac{1}{2}}$	1403	measured: see Tables 4,5,7
Si II	2	$3s^23p-3s^24s$	$^2P_{\frac{1}{2}}-^2S$	1527	measured: see Tables 4,5,7
Si II*	2		$^2P_{\frac{3}{2}}-^2S$	1533	
C IV	1	2s-2p	$^2S-^2P$	1548,1551	measured: see Tables 4,5,7
Fe II	8	a - y	$^6D_{\frac{9}{2}}-^6P$	1608	measured: see Tables 4,5
Fe II*	8		$^6D_{\frac{7}{2}}-^6P$	1618,1622	blended with above
Fe II*	8		$^6D_{\frac{5,3}{2\ 2}}-^6P$	1626-1636	possibly present?
Fe II*	8		$^6D_{\frac{1}{2}}-^6P$	1639	possibly present, blend with He II**?
He II**	12.01	2s-3p	$^2S-^2P$	1640	λ measured: see Table 7
Aℓ II	2	$3s^2-3s3p$	$^1S-^1P$	1671	seen (?) against O III em
Aℓ II**	6	3s3p-3s3d	$^3P-^3D$	1720-1725	possibly present
Aℓ II**	5	$3s3p-3p^2$	$^3P-^3P$	1764-1768	possibly present
Si II	1	$3s^23p-3s3p^2$	$^2P_{\frac{1}{2}}-^2D$	1808	present - see Footnote (1)
Si II*	1		$^2P_{\frac{3}{2}}-^2D$	1817	present - see Footnote (1) and Table 7
Aℓ III	1	3s-3p	$^2S-^2P$	1855, 1863	measured: see Tables 4,5,7
Aℓ II**	4	3s3p-3s4s	$^3P-^3S$	1856-1862	blended with above, possibly present: see Figure 2
Fe II	2	a - z	$^6D_{\frac{9}{2}}-^6F$	2374,2382	present: see Figure 2
Fe II*	2		$^6D_{J\leftarrow\frac{7}{2}}-^6F$	2383-2413	present: see Figure 2

Table 3 – *continued*

Multiplet(UV)		Transitions		λ(Å)	Measurements and Comments
Fe II	1	a - z	$^6D_{\frac{9}{2}}$-$^6D_{\frac{7}{2}}$	2585	present: see Footnote (2)
Fe II	1		$^6D_{\frac{9}{2}}$-$^6D_{\frac{9}{2}}$	2599	measured: see Tables 4,5
Fe II*	1		^{6}D-^{6}D	2598-2631	present: see Figure 2
He I**	13	2s-7p	^{3}S-^{3}P	2764	probably detected
Mg II	1	3s-3p	^{2}S-^{2}P	2796,2803	measured: see Tables 4,5
He I**	12	2s-6p	^{3}S-^{3}P	2829	present
Mg I	1	3s^2-3s3p	^{1}S-^{1}P	2852	present
He I**	11	2s-5p	^{3}S-^{3}P	2945	measured: see Table 4,5
He I**	Opt.3	2s-4p	^{3}S-^{3}P	3188	present

(1) Si II and Si II* λλ1808, 1816 measurements: 1979 May 3, W_λ (1808)=0.5±0.2, W_λ (1816)=0.6±0.3; 1979 June 1, W_λ (1808)=0.6±0.2, W_λ (1816)=0.3±0.3.

(2) Fe II λ2585 measurements: 1978 November 1, W_λ (2585)=0.9 Å, $DR=2(^{+2}_{-1})$; 1979 December 7, W_λ (2585)=1.2 Å, $DR=1.3(^{+0.4}_{-0.2})$, [*cf.* unsaturated doublet ratio . . . 3.5]. At all other epochs, a reseau masks the λ2585 line.

defined in Table 2 are both strong enough and sufficiently clear of spectral obstacles to provide useful data for detailed statistical analyses.

The difficulties involved in measuring absorption lines in NGC 4151 spectra have been discussed in Paper I. However, here the features have consistent definitions which avoid as far as possible any distorting factors. Some of the lines reported in table 4 of Paper I have been remeasured with the new, standard definitions.

Two quantities have been measured throughout:

(i) equivalent width,

$$W_\lambda = \sum_i [1 - F_i/F_c(i)]\,\delta\lambda_i \qquad (1)$$

(ii) relative effective wavelength $\Delta\lambda = \lambda_{obs} - \lambda_{lab}$ where λ_{lab} is a reference wavelength (see Table 2) and λ_{obs} is heliocentric observed wavelength,

$$\lambda_{obs} = \sum_i \lambda_i [1 - F_i/F_c(i)] \Big/ \sum_i [1 - F_i/F_c(i)] \qquad (2)$$

where the summation region is given in Table 2; $\delta\lambda_i$ is the sampling bin width (usually 2.67 Å for SWP and 4.4 Å for LWR, and constant over a line); and F_i and $F_c(i)$ are the values of flux respectively in the line and local continuum (defined in Table 2) at the wavelength λ_i of the ith bin. The wavelength scale for λ_{obs} is based on assuming certain emission lines are at a redshift $z=0.0033$ (see Paper I for details).

[*Note:* For the Si IV resonance doublet at λ1400, which is resolved even at low dispersion, two different definitions of the absorption feature have been made, for comparison purposes. One is

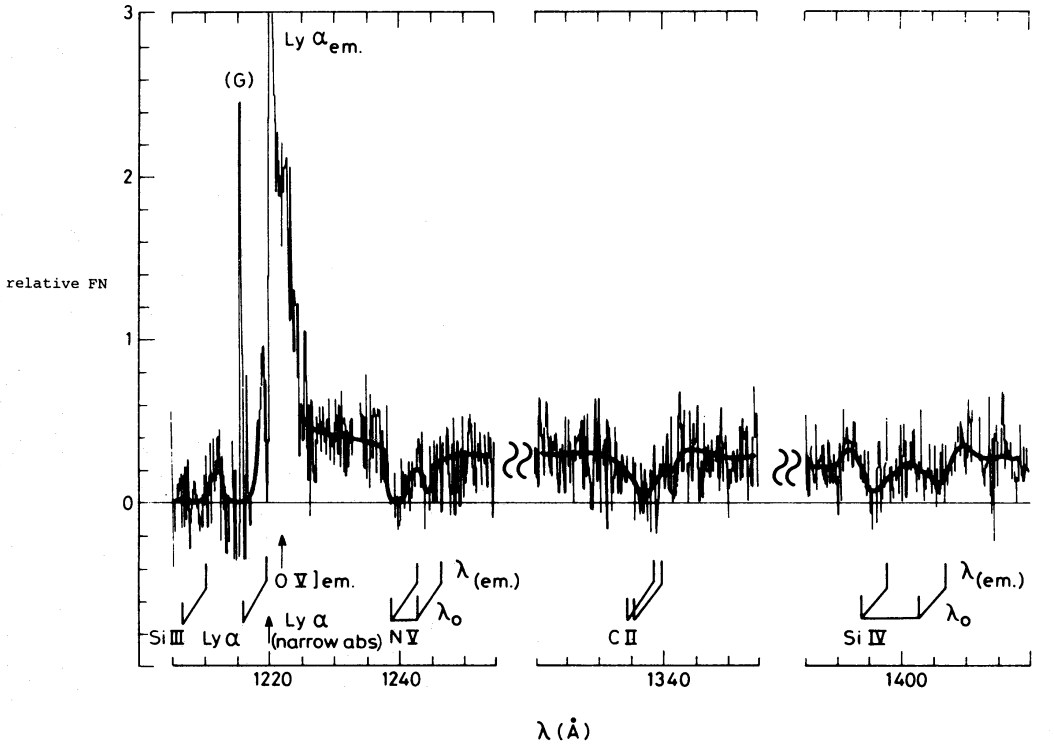

(a)

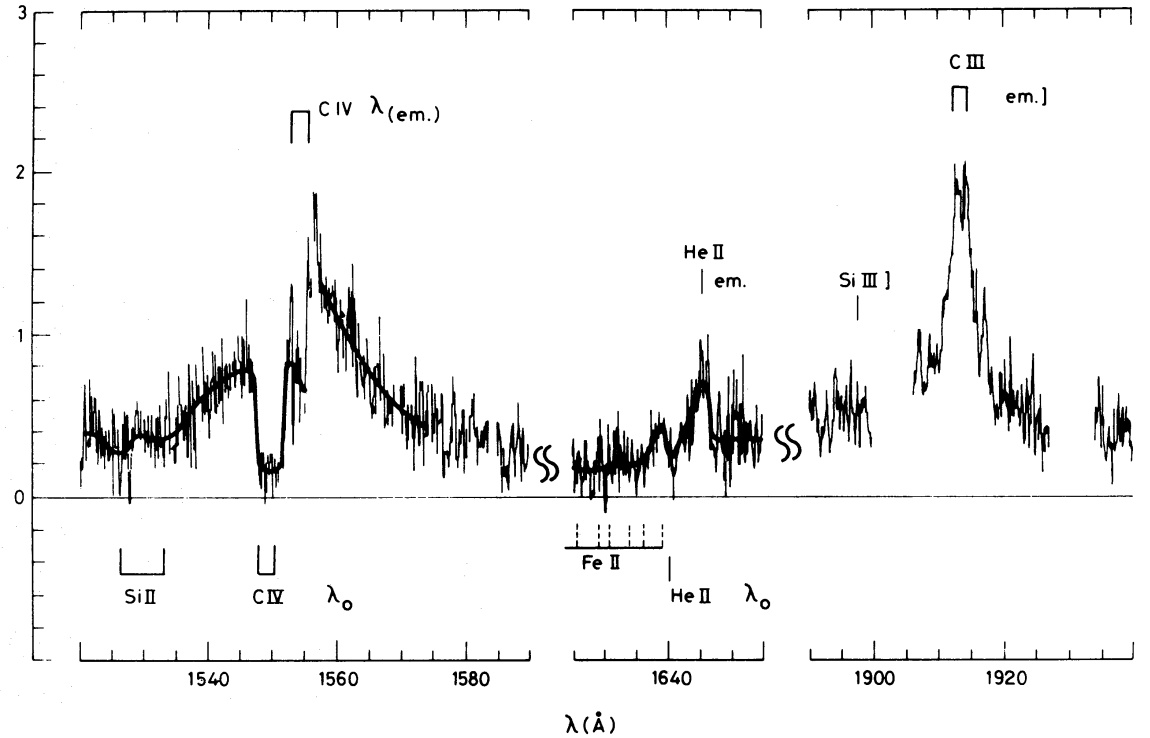

(b)

Figure 1. Extracts of mean high-dispersion spectrum for the 'high state' of NGC 4151 nucleus (average of 1978 August 2, October 24, 1979 May 20 and 26).

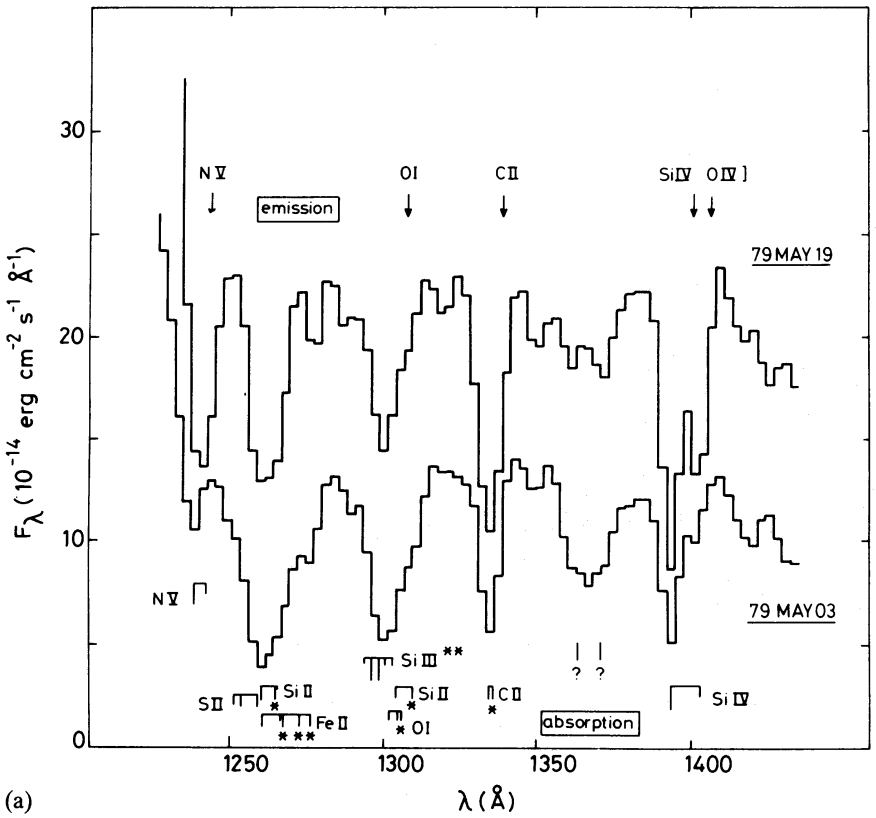

(a)

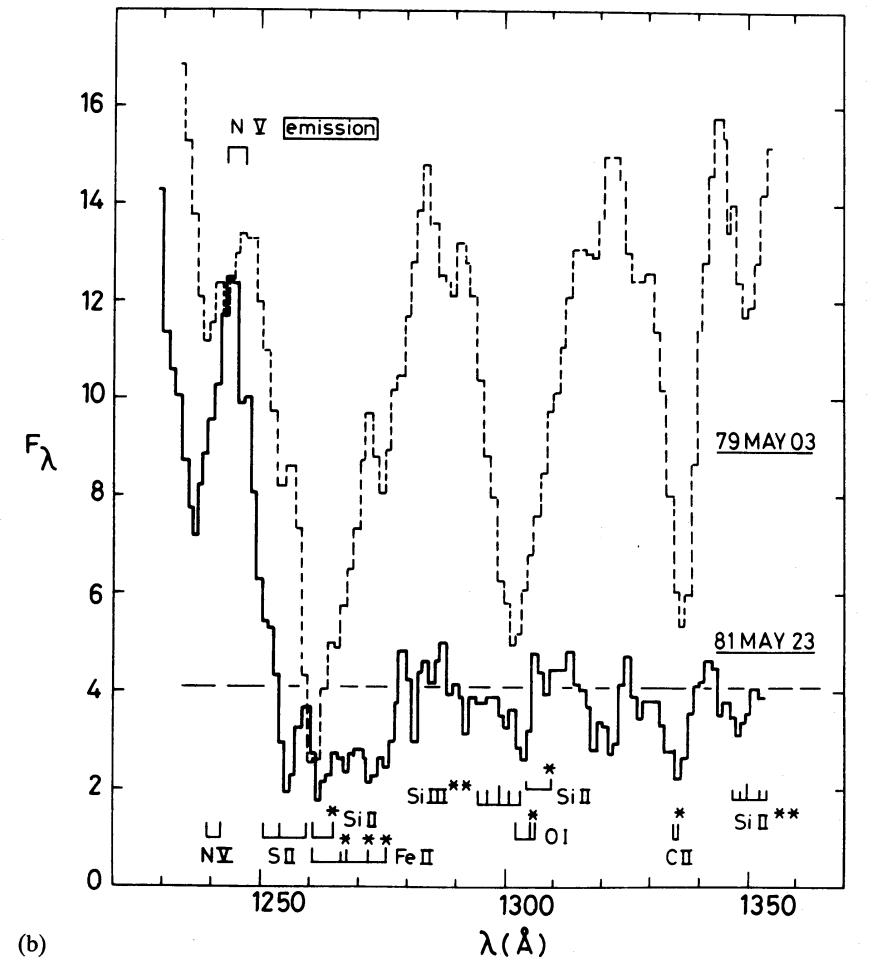

(b)

Figure 2. (a–e) Extracts of representative low-dispersion spectra: 1981 May 23 was 'very low state', 1979 May 3 'pre-flare state', 1979 May 19 approaching 'flare maximum' phase, and 1978 May a 'very high' state. Definite and possible absorption line identifications are indicated, together with positions of identified or expected broad emission lines. (R=reseau, G=geocoronal.)

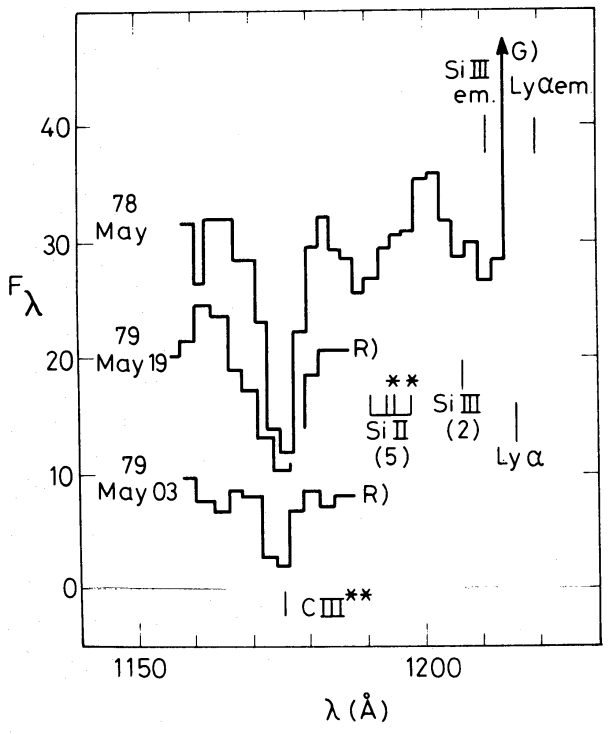

(c)

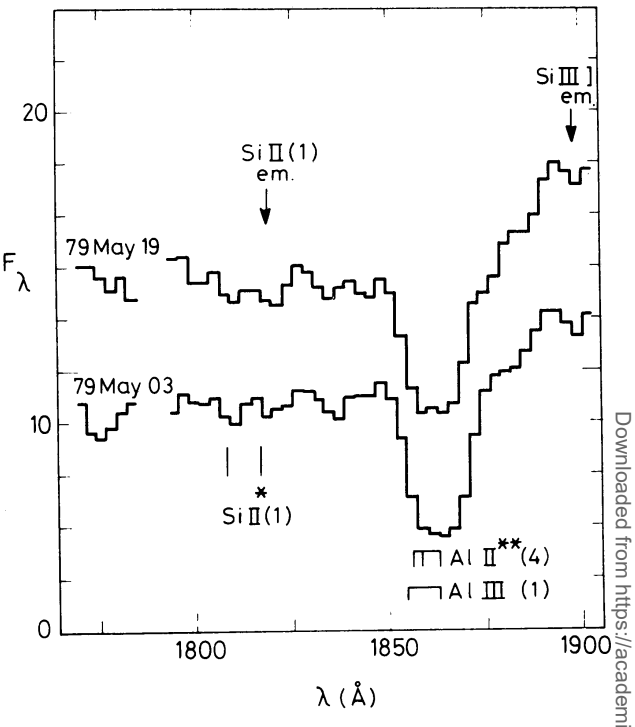

(d)

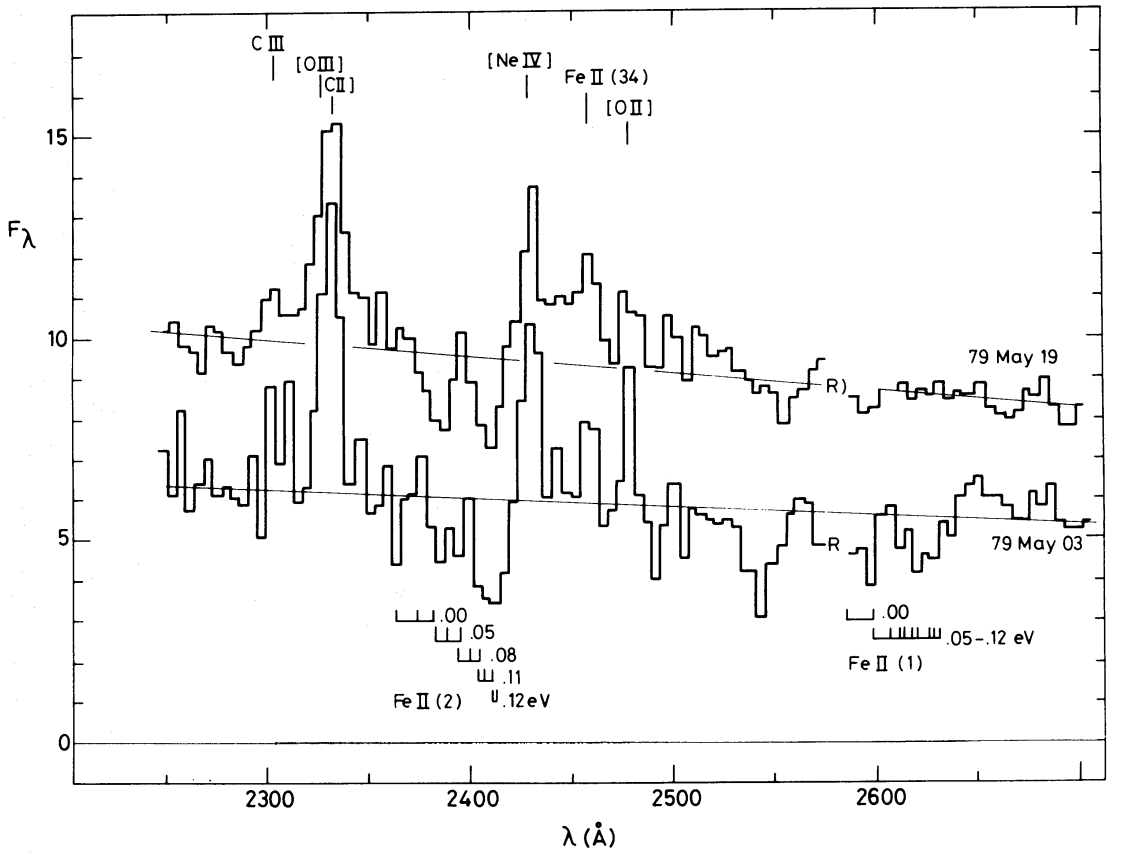

(e)

Figure 2 – *continued*

Table 4. Equivalent widths W_λ (Å) measured from low-dispersion spectra.

For definitions of features measured, see Table 2.

(a) Results for 1978–1980 May epochs, for 8 low-ionization features (arranged in order of increasing I.P. of likely major contributor).

Epoch	Event Label	Continuum flux F_ν (mJy) (± 0.4 typically)‡ (λ1455)	(λ2500)	Mg II λ2800 (LLC)	Fe II λ1608	Fe II λ2599	Si II+ λ1260	Si II λ1530	Si II λ1190	Al III+ λ1860	(unident) λ1370
1978											
Feb 28.7		13.4:	N	N	W	N	1.5±1.5	W	W	2.0±1.0	W
Apr 16.9		15.8	21.8:	S	0.8±0.4	1.2±0.4	2.2±0.5	0.9±0.4	R	4.5±1.4	-0.1±0.5
May 8–12		(15.1)	(23.5)	2.2±1.3	0.4±0.3	1.8±0.5	0.8±0.3	0.8±0.5	1.0±0.3	1.0±0.6	-0.1±0.5
Jun 17.6		(11.8)	N	N	0.4±0.4	N	1.2±0.5	1.4±0.5	0.7±0.6	2.5±1.0	0.0±0.5
Jul 24.29		10.9	16.7	2.5±1.5	0.6±0.4	1.5±0.9	4.8±0.7	W	1.8±0.4	4.3±0.6	0.4±0.6
Aug 02.1		9.5	N	N	W	N	4.6±0.8	1.5±0.6	R	2.8±0.9	0.3±0.6
Oct 19.7	D1	9.6	18.8	3.9±1.0	0.2±0.3	1.7±0.5	3.2±0.5	1.1±0.6	1.5±0.4	3.0±0.6	-0.3±0.6
Nov 01.0	D1	(4.3)	(11.3)	2.8±1.4	0.6±0.4	2.0±1.0	7.8±0.8	1.0±0.5	3.6±0.7	5.8±1.1	0.0±0.5
Dec 09.5		8.3	15.2	3.1±0.9	0.0±0.4	0.8±0.4	3.5±0.5	W	1.5±0.5	3.0±0.6	0.0±0.5
1979											
Jan 21.6		5.4	11.0	2.9±1.0	1.4±0.4	1.5±0.7	5.0±0.7	1.3±0.5	R	4.2±0.9	1.6±0.6
May 03.3	I1	8.1	10.8	3.3±1.0	2.1±0.4	1.7±0.8	12.7±0.6	2.6±0.3	R	9.3±0.8	4.7±0.5
May 04.6	I1	7.0	N	N	W	N	13.7±1.0	2.3±0.5	R	8.9±1.1	6.1±1.0
May 19.2	I1	12.5	17.7	3.8±0.6	0.8±0.2	0.5±0.2	4.5±0.5	0.8±0.3	R	5.9±0.6	1.6±0.4
May 21.3	I1	13.6	19.4	2.8±1.0	0.8±0.2	0.7±0.4	3.8±0.5	1.2±0.4	R	4.9±0.8	0.5±0.5
May 23.1	(I1)	13.1	19.0	4.6±0.8	0.9±0.2	0.6±0.2	4.1±0.5	0.8±0.4	R	6.0±0.8	0.6±0.5
May 25.1	(I1)	13.7	20.0	3.9±0.8	0.7±0.2	0.8±0.3	3.8±0.5	1.4±0.4	R	4.1±0.8	0.8±0.5
May 31.7	(I1)	13.6	N	N	0.8±0.4	N	2.9±0.8	0.7±0.5	R	3.7±1.0	1.1±0.8
Jun 01.2	(I1)	13.6	20.4	2.9±0.6	0.8±0.2	1.1±0.4	3.6±0.4	1.0±0.4	R	4.0±0.8	0.0±0.4
Aug 07.9		8.9	11.9	3.4±0.5	1.1±0.2	1.3±0.2	5.7±0.6	1.3±0.3	R	4.9±0.7	0.3±0.4
Dec 07.9	D2	11.2	16.0	3.8±0.7	0.5±0.2	1.6±0.3	4.1±0.6	1.4±0.4	2.2±0.5	4.0±0.7	0.8±0.6
Dec 12.7	D2	8.7	13.5	4.0±1.2	0.6±0.4	2.2±0.9	5.8±0.6	1.2±0.4	2.9±0.5	5.4±0.8	0.2±0.5
Dec 13.5	(D2)	8.7	13.5	4.0±0.8	1.1±0.3	0.9±0.4	5.6±0.6	1.1±0.3	R	5.7±0.8	0.3±0.5
Dec 14.0	(D2)	9.9	N	N	1.9±0.6	N	3.5±0.8	1.2±0.5	R	6.3±0.9	2.4±1.0
1980											
Jan 01.4		8.5	13.3	3.6±1.0	0.2±0.4	1.4±0.6	6.4±0.7	1.4±0.4	1.7±0.4	4.8±0.7	0.3±0.5
Mar 01.4	I2	7.2	11.0	4.0±1.5	1.0±0.6	0.7±0.5	10.0±0.9	1.5±0.4	R	7.3±0.9	1.9±0.8
Mar 04.2	I2	7.8	11.2	4.9±1.6	0.4±0.5	0.2±0.5	9.8±1.0	1.6±0.4	R	7.6±0.9	1.6±0.8
Mar 04.8	I2	8.2	N	N	1.9±0.7	N	10.2±1.0	1.6±0.4	R	6.6±0.8	2.0±0.8
Mar 06.2	I2	9.3	12.9	5.2±1.6	0.9±0.6	0.7±0.5	8.7±0.8	1.7±0.4	R	7.4±0.9	0.5±0.9
Apr 21.2	(I3)	2.6	6.5	2.7±2.0	2.2±1.2	1.1±0.7	3.8±1.5	W	W	4.2±1.7	0.6±0.5
May 15.0	I3	12.7	14.8	2.9±1.2	1.0±0.5	1.0±0.8	6.7±0.7	1.1±0.4	R	6.1±0.9	1.6±0.8
May 19.3	I3	12.4	17.9	3.7±0.9	0.5±0.3	1.7±0.5	5.0±0.5	1.4±0.4	R	5.0±0.7	0.6±0.6

Table 4 – *continued*

(b) Results for same 1978–1980 May epochs as in Table 4(a) but for 8 intermediate- to high-ionisation absorption features

Epoch	Event Label	Continuum flux F_ν(mJy) (±0.4 typically)‡ (λ1455)	(λ2500)	C II λ1335	He I** λ2945	Si III+** λ1300	Si IV λ1394 (LLC)	Si IV λ1402 (LLC)	C III** λ1175	C IV λ1550 (LLC)	N V λ1240 (LLC)
1978											
Feb 28.7		13.4:	N	3.0±1.0	N	W	3.0±1.2	1.5±0.9	4.0±2.5	3.0±0.8	6.0±1.0
Apr 16.9		15.8	21.8:	2.3±0.6	-0.8±0.6	1.8±0.5	4.0±1.0	2.1±0.8	2.5±0.9	2.9±0.5	6.0±0.7
May 8–12		(15.1)	(23.5)	1.9±0.4	0.2±0.5	1.4±0.4	3.3±0.8	1.6±0.5	3.6±0.5	3.6±0.5	6.9±0.6
Jun 17.6		(11.8)	N	1.6±0.7	N	0.6±0.4	2.2±1.3	1.4±1.0	2.3±1.0	3.8±0.5	6.0±0.7
Jul 24.29		10.9	16.7	3.1±0.5	W	1.3±0.4	3.7±1.0	2.1±0.6	3.1±1.2	3.5±0.5	4.1±0.6
Aug 02.1		9.5	N	3.6±0.6	N	1.2±0.5	4.4±1.3	1.8±1.0	W	2.7±0.7	3.4±0.7
Oct 19.7	D1	9.6	18.8	2.6±0.4	0.2±0.4	1.4±0.4	5.0±1.0	2.5±0.7	3.7±1.4	3.6±0.4	5.6±0.5
Nov 01.0	D1	(4.3)	(11.3)	1.2±1.0	0.8±0.6	1.7±0.8	1.8±1.4	0.8±0.8	4.1±1.5	3.3±0.8	4.3±0.7
Dec 09.5		8.3	15.2	2.8±0.4	0.9±0.5	3.5±1.1	3.8±0.9	1.7±0.7	5.0±1.5	3.1±0.5	5.6±0.5
1979											
Jan 21.6		5.4	11.0	2.6±0.4	1.0±0.6	1.9±0.7	2.2±0.8	0.6±0.5	5.0±1.1	2.8±0.4	4.0±0.6
May 03.3	I1	8.1	10.8	4.1±0.3	1.3±0.5	7.6±0.9	4.0±0.8	1.1±0.6	4.1±0.7	3.1±0.4	1.6±0.5
May 04.6	I1	7.0	N	4.5±1.0	N	6.8±1.0	5.9±1.7	3.6±1.4	4.9±1.6	4.1±0.8	2.2±0.8
May 19.2	I1	12.5	17.7	4.2±0.3	1.2±0.4	3.4±0.5	4.4±0.6	2.9±0.4	4.6±0.6	4.3±0.3	5.5±0.4
May 21.3	I1	13.6	19.4	3.7±0.3	0.5±0.6	2.5±0.3	4.9±0.8	3.2±0.6	3.8±0.4	4.3±0.3	6.3±0.5
May 23.1	(I1)	13.1	19.0	3.9±0.3	1.1±0.4	2.3±0.4	4.7±0.8	2.9±0.6	2.9±0.8	4.4±0.5	6.0±0.5
May 25.1	(I1)	13.7	20.0	3.5±0.3	0.7±0.5	2.3±0.4	4.7±0.8	3.0±0.6	3.9±0.5	4.3±0.5	6.0±0.5
May 31.7	(I1)	13.6	N	2.8±0.5	N	1.4±0.5	5.0±1.1	3.2±0.8	3.7±0.7	4.0±0.6	6.8±0.6
Jun 01.2	(I1)	13.6	20.4	3.5±0.3	1.0±0.4	1.2±0.6	4.9±0.6	3.0±0.4	2.6±0.5	4.7±0.3	6.2±0.4
Aug 07.9		8.9	11.9	3.1±0.4	0.8±0.3	1.9±0.8	4.3±0.7	1.6±0.4	3.6±0.4	3.8±0.3	3.8±0.4
Dec 07.9	D2	11.2	16.0	3.2±0.3	0.7±0.4	1.0±0.4	3.3±0.9	1.9±0.6	2.6±0.7	4.2±0.3	5.3±0.4
Dec 12.7	D2	8.7	13.5	3.6±0.3	0.6±0.5	2.8±0.4	2.9±0.8	1.6±0.5	4.5±1.3	4.2±0.4	5.2±0.5
Dec 13.5	(D2)	8.7	13.5	3.7±0.3	0.5±0.5	2.6±0.5	3.9±0.8	2.1±0.6	6.0±1.1	4.4±0.4	4.8±0.5
Dec 14.0	(D2)	9.9	N	4.0±0.5	N	1.2±0.5	3.6±1.0	3.0±0.8	5.5±1.6	4.5±0.6	5.1±0.6
1980											
Jan 01.4		8.5	13.3	3.4±0.3	0.8±0.4	0.6±0.5	3.3±0.8	1.1±0.6	3.3±1.2	4.2±0.4	4.5±0.5
Mar 01.4	I2	7.2	11.0	4.3±0.5	1.9±0.9	2.5±0.5	4.0±1.1	1.7±0.9	3.1±1.2	3.5±0.5	2.3±0.6
Mar 04.2	I2	7.8	11.2	3.4±0.5	0.4±0.7	4.2±0.6	4.1±1.1	1.6±0.9	3.3±1.1	4.1±0.5	3.6±0.6
Mar 04.8	I2	8.2	N	3.8±0.5	N	4.0±0.6	4.5±1.2	1.5±0.8	3.7±1.1	3.5±0.5	4.0±0.6
Mar 06.2	I2	9.3	12.9	5.3±0.5	1.5±0.9	2.7±0.5	4.0±1.1	1.7±0.9	4.7±1.0	3.4±0.5	4.0±0.6
Apr 21.2	(I3)	2.6	6.5	2.5±1.5	0.8±1.0	0.7±1.0	1.2±0.8	0.4±0.5	W	3.5±0.6	0.5±0.5
May 15.0	I3	12.7	14.8	4.7±0.5	1.7±0.8	4.3±0.6	4.6±1.2	3.5±1.0	4.0±0.8	3.3±0.5	4.0±0.6
May 19.3	I3	12.4	17.9	4.2±0.4	0.8±0.9	3.4±0.4	4.5±0.9	2.8±0.7	5.2±0.7	3.0±0.4	5.3±0.5

Table 4 – *continued*

(c) Additional measurements for selected 1980 Jul–1981 Jul ("very low state") epochs including newly-derived continuum fluxes F_ν (mJy) calculated in the same way as those in Paper II.

Epoch	F_ν (mJy)		W_λ (Å) For Features Defined in Table 2				
	λ 1455 Å	λ 2500 Å	Si II+ λ 1260	Si II λ 1530	C II λ 1335	Si III+ λ 1300	C IV λ 1550
1980							
Jul 30.5	6.0±.6	N	4.2	2.9	3.3	1.9	3.1
Nov 27.5	2.1±.3	4.4±.3	2.0:	0.5:	1.8	<1:	<1.0:
1981							
Apr 26.4	2.0±.3	4.0±.2	2.5:	2.0:	1.6	<1:	2.8
May 08.1	1.9±.2	3.8±.2	3.1	1.2	1.7	0.7	1.6
May 23.2	2.5±.2	4.9±.2	5.3	2.3	1.7	1.5	2.6
Jun 05.2	2.5±.2	4.4±.3	6.0	2.0	<1:	<1:	2.7
Jun 09.0	2.2±.2	4.6±.2	3.4	2.1	1.6	<1:	2.6
Jun 26.0	2.4±.4	N	6.6	2.4	1.0	<1:	3.1
Jun 28.0	2.0±.4	N	5.1	2.6	1.8	0:	2.4
Jun 30.0	2.6±.3	4.7±.2	3.5	2.5	0.9	1.0	2.9
Jul 16.9	2.1±.3	3.9±.2	3.0	1.5	0.9	<1:	2.6
Average Estimated Standard Errors =			±2.	±1.	±0.5	±1.	±1.

Key:
N No spectrum obtained in this λ range.
R Camera reseau masks feature.
S Spectrum saturated at this λ.
W Spectrum too weak or noisy to measure feature.
(LLC) These features defined with a 'low local continuum' estimate – true W_λ is larger but difficult to define objectively and consistently (see Table 2).
‡For details of continuum flux determinations and errors, see Paper II.

based on a 'low local continuum' (LLC) where (as for Nv, Civ and Mgii) a local continuum is drawn simply as a straight line joining the apparent emission maxima to either side. This gives lower limits on equivalent widths, and overestimates the observed Siiv doublet ratio (giving a ratio greater than 2.5 in a quarter of the cases, compared with the physical upper-limit of 2.0). The alternative definition uses a 'high local continuum' (HLC) which simulates the broad underlying Siiv + Oiv emission by a simple parameterization. The line is defined by the observed wings over λλ1350–1382 and 1412–1430 Å and a Doppler core with FWHM=4000 km s^{-1} centred at λ1402±1 Å. HLC equivalent widths and doublet ratios are more realistic than the LLC ones, and have been used when estimating velocity 'b' parameters and column densities. However, for

detailed correlation analyses and comparisons with N v and C iv (for which only LLC measurements were feasible) the Si iv LLC values were used.]

The results for equivalent widths W_λ and relative wavelengths $\Delta\lambda$ are listed in Tables 4 and 5 respectively. The uncertainties quoted in these tables were carefully evaluated, as explained in Appendix A of this paper. Additional information on velocities was obtained from the high-dispersion spectra (see Section 3.3 below).

Graphs of W_λ versus time are shown in Fig. 3, together with the light curve of F_ν(2500 Å) continuum flux for comparison. The flare (I) and decay (D) events discussed in Paper II are labelled in this figure. It can be seen from Fig. 3 that there is a striking, detailed correlation between the equivalent width of N v (the highest ionization species measurable with *IUE*) and the continuum flux at 2500 Å. Equally striking is the persistent *anti*-correlation of continuum flux with equivalent widths of *low* ions such as Si ii. This behaviour is most clearly seen in the development of flare event I1 (1979 May). The correlations are discussed in detail in Section 4 below.

At the 'very low state' epochs [F(1455 Å)<3 mJy] all absorption lines seem weak. This suggests there is a continuum component present at all times, that is *not* covered by absorbers. This component tallies with the small remaining short-wave excess present even at 'anomalous' epochs (Paper III), and is attributable to stars or jets outside of the BLR.

3.3 ADDITIONAL VELOCITY MEASUREMENTS FROM HIGH-DISPERSION DATA

With the exception of C iv, it is difficult to measure absorption velocities on the *individual* high-dispersion spectra, because of the low signal-to-noise. However, the C iv lines are clearly seen against the corresponding emission. Nevertheless, the short-wavelength edge of the weaker λ1550.77 line is lost in the stronger λ1548.20 absorption, and in addition the apparent long-wavelength edge of λ1548.20 may be caused or distorted by an overlying emission component from the narrow line region (Penston *et al.* 1979).

Table 6 gives information concerning the profile of the C iv absorption at the five high-dispersion epochs. Estimates of velocities of the overall 'blue' edge of the absorption feature, and 'red' edges for both components of the doublet, are given with respect to that of the Lyα geocoronal emission, thus taking into account any spurious wavelength scale shifts in the extracted spectra. This wavelength scale is satisfactory in that it leads to no significant velocity changes (within the measuring errors of $\pm 30\,\mathrm{km\,s^{-1}}$)] in either the narrow Lyα absorption which arises in the outer parts of NGC 4151, or the C iii]$\lambda\lambda$1907/9 emission feature which is dominated by the narrow line region (*cf.* Penston *et al.* 1979). Table 6 also gives the minimum residual intensity in each component of the C iv absorption doublet, and an indication of which part of the line profile shows this greatest absorption.

It can be seen that the range of velocities covered by the line is remarkably constant except at 1978 December 25, an epoch when NGC 4151 was faint. This change is quite significant ($\sim 120\,\mathrm{km\,s^{-1}}$) and can be seen by inspection of the profiles (see fig. 1 of Penston *et al.* 1979). Even so, the width and blueshifted character of the line is similar from epoch to epoch and it is apparent that changes in the equivalent width arise more through changes in the depth of the line (and thus presumably the column of C^{+++} ions) than in the velocity range spanned. The low-resolution data provide further evidence of this (see Section 5 below).

In order to study any variations in velocities with ionization state, at improved signal-to-noise, an average high-state high-dispersion spectrum was constructed from the data for 1978 August 2, October 23 and 1979 May 20 and 26. Now, at these four epochs the C iv absorption lines were almost identical in velocity and strength (see Table 6). Proceeding on the assumption that this was also true (at least approximately) for all other lines, the approximate velocity ranges covered by various ion species were estimated from the mean spectrum. These are given in Table 7.

Table 5. Relative wavelengths of absorption lines, measured from low-dispersion spectra. For definitions of features measured, see Table 2.

Values tabulated here are $\Delta\lambda(\text{Å}) = \lambda_{obs} - \lambda_{lab}$ (where λ_{lab} is the reference wavelength)

Epoch	Event Label	Id=Mg II λ_{lab}=2797.9	Fe II 1608.5	Fe II 2599.4	Si II+ 1260.4	Si II 1526.7	Si II 1191.9	Al III+ 1857.4	(?) 1368.0	C II 1334.5	He I** 2945.1	Si III+** 1303.3	Si IV Mean of 2 Lines	C III** 1175.7	C IV 1549.1	N V 1240.1
1978																
Feb 28.7		N	W	N	W	W	W	W	W	+2.3:	N	W	W	+1:	+0.9:	+1.4:
Apr 16.9		S	-1	-1	+2.7	-1.7:	R	+5	W	-0.6	W	-3.4	-0.2	-0	+0.2	+1.6
May 8-12		+4	+3	-3	+3.2:	W	+0.3:	+2	W	+1.7:	W	-1.2	+2.5:	+2:	+1.8:	+2.4:
Jun 17.6		N	+1	N	+2.2	-2.0:	+2.4	+4:	W	-0.3	N	-4.4	+1.2	+2	+3.4:	+2.9:
Jul 24.9		-1	+1	+1	+6.1:	W	+3.6	+6	-2:	+2.3	W	+0.4	+1.2	+3	+1.7	+1.2
Aug 02.1		N	W	N	+2.9	+1.0:	R	+4	W	+1.6	N	-1.7	+0.2	W	+0.1	+1.3
Oct 19.7	D1	-1	+1	-0	+3.6	+0.8:	+0.9	+3	W	+0.3	+1:	-2.8	+0.1	-1	+0.2	+1.1
Nov 01.0	D1	+1	-0	-1	+5.1	+0.8:	+3.0	+5	W	+0.8:	W	-1.3:	+1.9:	+1	+2.5:	+1.4
Dec 09.5		-0	W	+2	+5.3	W	+4.1	+4	W	+0.5	+3	-3.7	+0.2	+2	+0.6	+1.2
1979																
Jan 21.6		-0	+0	-4	+3.6	W	R	+1	-2	+0.5	W	-3.0	+0.8:	-0	-0.1	+1.1
May 03.3	I1	-1	-0	-4	+3.6	+0.6	R	+5	-1.4	+0.1	-1	-1.3	-0.3	-4	-1.8	-1.6
May 04.6	I1	N	W	N	+4.8	+0.3	R	+6	-1.7	+1.4	N	-0.8	-0.2:	-3	-0.5:	+0.1
May 19.2	I1	-0	-1	-3	+1.7	-2.2	R	+5	-1	+0.7	+4	-2.2	+0.5	-2	-0.5	+1.0
May 21.3	I1	+3	+1	-1	+2.3	-0.2	R	+4	-1:	+0.8	+3	-4.4	+0.6	+0	+0.1	+1.0
May 23.1	(I1)	+1	+1	-1	+1.7	-1.7	R	+4	-5	+0.2	-0	-3.0	+0.2	-1	-0.5	+1.0
May 25.1	(I1)	+2	+0	-2	+1.3	-1.5	R	+4	-5	-0.1	+6:	-3.5	+0.5	-1	-0.3	+1.0
May 31.7	(I1)	N	+4	N	+0.6	-1.9	R	+4	-5	+0.1	N	-4.3	+0.5	-3	+0.1	+2.0
Jun 01.2	(I1)	+0	-1	-2	+1.6	-2.3	R	+4	W	+0.5	+5:	-3.1:	-0.2	-1	-0.3	+1.2

Aug 07.9		+2	+1	-2	+2.2	-1.6	R	+5	W	+0.8	+1	-1.3:	-0.1	+1	-0.7	+0.7
Dec 07.9	D2	-2	+2	-2	+2.7	-0.8	-0.1	+5	-2	0.0	-2:	-1.5	+0.4	-2	+0.1	+1.0
Dec 12.7	D2	+2	+1	+1:	+2.5	-1.7	+2.5	+6	W	+1.1	+6:	-4.1	+0.5	-1	+1.4	+1.1
Dec 13.5	(D2)	+3	+0	-2	+2.5	-1.3	R	+5	W	+1.3	+6:	-0.1	+0.6	-2	+0.0	+1.1
Dec 14.0	(D2)	N	+0	N	+2.4	-0.9	R	+4	+1	+1.7	N	-1.0	+0.8	-3	+0.4	+1.7
1980																
Jan 01.4		-0	+2:	-2	+2.7	-0.5	+3.4	+5	-3:	+1.7	+5	+1.0	+0.2	-0	+1.0	+1.1
Mar 01.4	(12)	+2	+2	-2:	+3.5	-0.6	R	+6	+0	+1.7	+3	-2.9	+0.4	+1	+0.1	-0.6
Mar 04.2	12	+3	+4	W	+3.8	-0.5	R	+6	+2	+0.7	W	-1.7	+0.3	+1:	-0.1	+0.6
Mar 04.8	12	N	+3	N	+1.6	+0.3	R	+5	-1	-0.2	N	-0.4:	-1.0	-1:	-0.9	+1.6
Mar 06.2	12	+4	+3:	+0	+1.6	-1.5	R	+6	+1	+2.0	+3	-0.7	-0.7	-3	+0.2	+0.1
Apr 21.2	(13)	+0	+3	-2:	+3.9:	W	W	+3:	W	-0.5:	W	W	W	W	-0.0	W
May 15.0	13	-0	+0	-1	+4.4	+1.9	R	+7	-1	+2.0	+4	-0.2	+0.7	-0	+1.1	+1.0
May 19.3	13	+1	+2	-3	+2.7	-0.1	R	+5	+1	+0.5	+4	-1.7	+0.6	-1	-0.3	+1.0
Uncertainty on Individual Entries (Average)	=	±3	±2	±2	±0.7	±1.5	±1.4	±2	±2	±0.7	±3	±1.4	±0.6	±2	±0.8	±0.8
Mean λ_{obs}(Å)	=	2798.9	1609.7	2597.9	1263.4	1525.8	1194.1	1862.0	1366.6	1335.4	2947.9	1301.3	1394.2 1403.2	1175.2	1549.4	1241.2
		±.8	±.6	±.6	±.5	±.4	±1.0	±.4	±.9	±.3	±1.2	±.5	±.3	±.6	±.4	±.4

For Key, and Continuum Fluxes at Each Epoch, See Table 4.

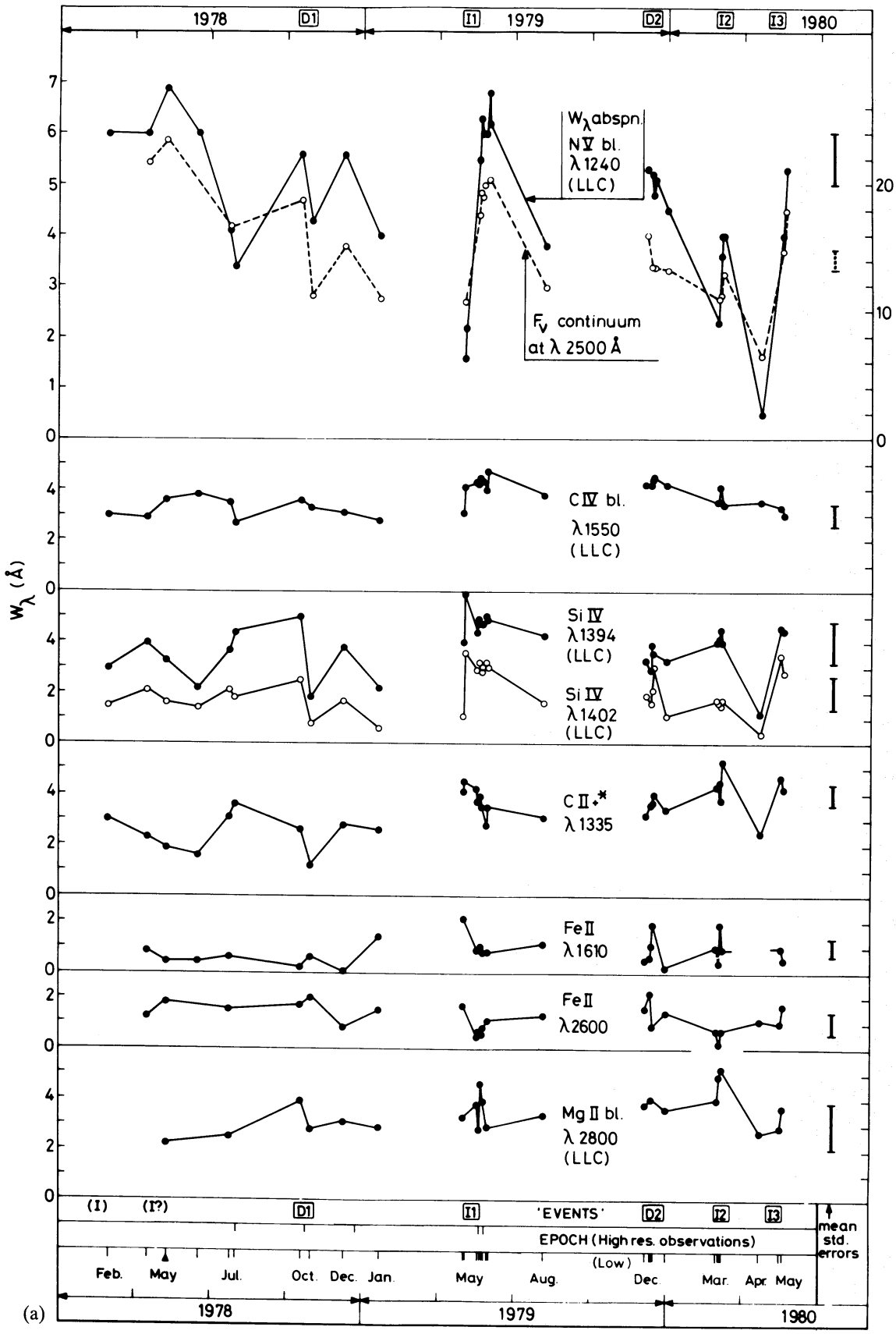

Figure 3. (a, b) Montage of curves showing time dependence of equivalent widths W_λ of all measured absorption lines, and also for direct comparison the λ 2500 continuum flux, for the main monitoring period 1978 February–1980 May. The epochs of both low- and high-resolution observations are indicated, as are the labelled 'events' D1, I1, etc. Points are joined by straight lines, for aiding the eye, but it should be emphasized that some 'events' may well have been missed with the uneven time-sampling.

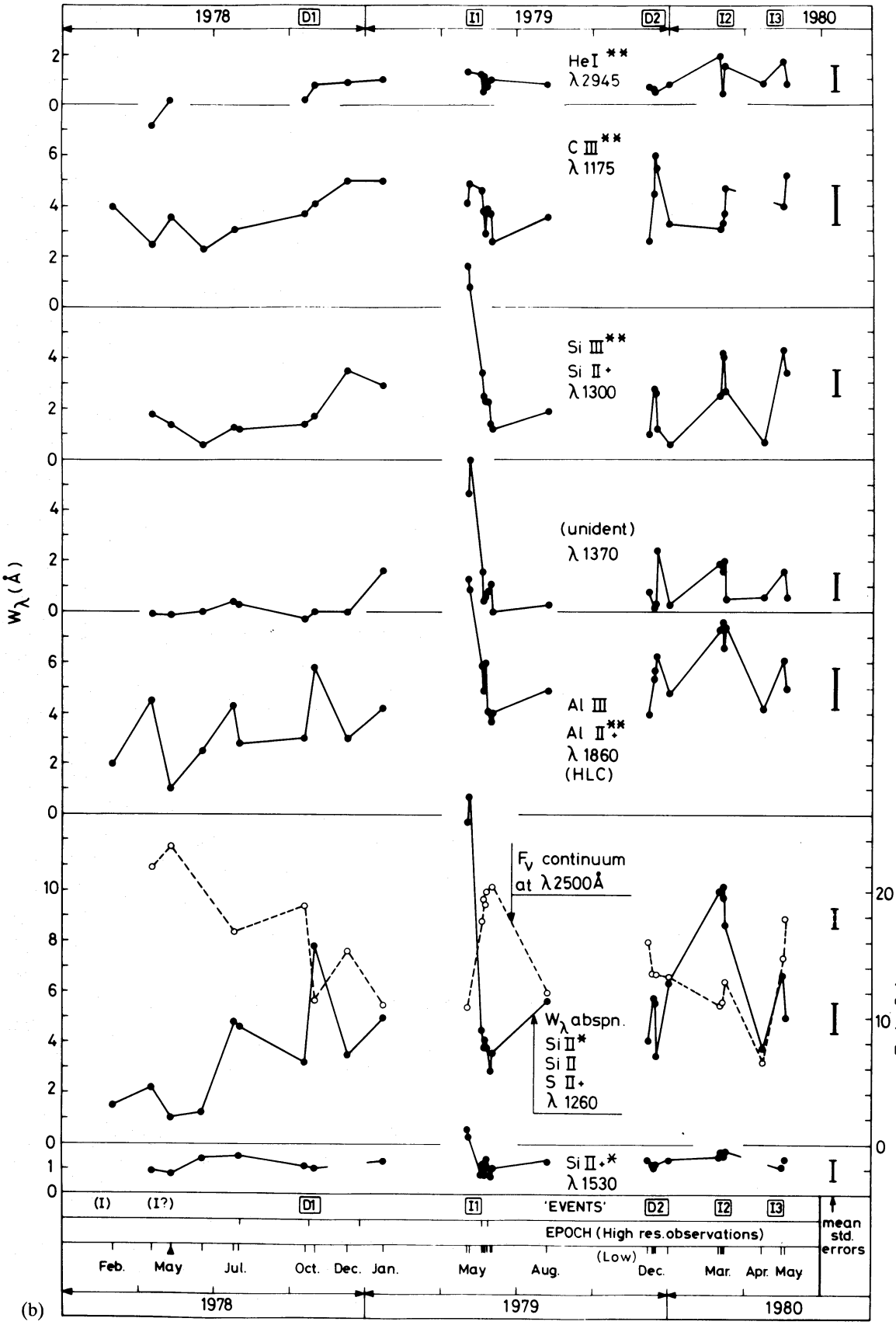

Figure 3 – *continued*

Table 6. Variation in C IV absorption profile in high-dispersion spectra.

date	velocities (km s^{-1})			residual intensities at absorption maxima	
	λ 1548.20 'blue' edge	λ 1548.20 'red' edge	λ 1550.77 'red' edge	λ 1548.20 (with relative position of deepest absorption)	λ 1550.77
1978 Aug 02	-150	760	860	0.1 (Red)	0.3
Oct 23	-120	760	930	0.0 (Red)	0.0
Dec 25	-300	670	770	0.3 (Centre)	0.7
1979 May 20	-160	700	840	0.0 (Blue)	0.5
May 26	-190	780	880	0.0 (Blue)	0.3

NOTES:

(1) The zero point of the IUE wavelength scale was established using the geocoronal Ly α line.

(2) Measurement errors are ~ 30 km s^{-1}.

(3) On 1978 Dec 25 the nucleus was faint; at the other four epochs it was bright (see optical magnitudes in Table 1; ultraviolet continua followed the same trend).

(4) The residual intensities were measured as fractions of the 'local continuum', that is, the emission line. The true continuum flux was approximately 0.2 times this local continuum.

It can be seen from Table 7 that there is no obvious dependence of velocities absorbed on excitation state. The only significant differences between the different lines lie in the estimates of the apparent 'redward' edge: the edge velocity seems to be lower when there is strong emission from that species. If this is a real effect, it could be a consequence of the different absorptions covering different proportions of continuum and emission line regions.

4 Results: correlations of equivalent widths, continuum flux, and wavelength shifts

In order to derive an overall picture of ionization conditions and velocities in the absorption line region, and their dependence on continuum flux, series of linear correlation tests were applied to all the F_ν, W_λ and $\Delta\lambda$ data from Tables 4(a, b) and 5 – that is, 16 features at the first 31 epochs. The effects of observational error were taken into account from estimated uncertainties on each individual measurement. Details are provided in Appendix B of this paper. whilst the most important and statistically significant results are described below.

[*Note*: Some of the *resonance* lines studied in this paper may have a constant, small contribution from 'interstellar' absorbers – in the disc and halo of our own Galaxy and in the outer regions of the NGC 4151 galaxy. It has not been possible to separate these from the BLR absorptions in the correlation analyses. However, of the lines studied in detail here (Table 2), even the lowest recorded equivalent widths of λλ 1610, 2600 (Fe II), λ 1300 (O I, Si II), λ 1530 (Si II) and λ 1260 (Si II, S II, Fe II) are still about twice the corresponding 'background' interstellar levels, assuming

Table 7. Ranges of velocity occupied by absorption in mean (high-dispersion) spectrum.

Line	Wavelength Å	Range of Velocity km s^{-1}	
Lα (Narrow)	1215.67	920	1020
Lα (Broad)	1215.67	X	1040 E
N V	1238.80	-150	680
N V	1242.78	220	630
S II	1259.53	- 10	B
Si II*	1265.04	- 10	610:
Si III**	1294.55	-150	B
Si II*	1309.28	B	>440 N
C II	1334.52	- 50	B
C II*	1335.68	B	>840 N
Si IV	1393.73	- 10	1240
Si IV	1402.73	+ 60:	1020:
Si II*	1533.44	-160	830:
C IV	1548.20	-160	780 E
C IV	1550.77	>290 B	890: E
He II**	1640.49	- 90	840 E
Si II*	1816.96	300	B
Si II*	1817.42	B	1250
Aℓ III	1854.72	- 80	1180:
Aℓ III	1862.78	120	680

NOTES:

The blue edge is generally sharper and easier to measure than the red one. Uncertainties are typically ± 50 to 100 km s^{-1}.

X No signal.

E Edge measured against emission peak.

B Line blended at this edge.

N Noise spike makes it impossible to define end.

column densities similar to those in the 3C 273 sightline (Ulrich *et al.* 1980). Furthermore, the velocities of the active nucleus material and of interstellar absorbers in our Galaxy overlap and cannot be separated by *IUE*, even in the high-resolution mode. As this overlap is caused by the intrinsic width of the broad absorption lines, a very much better signal-to-noise ratio than is possible with *IUE* is needed in order to attempt this separation.]

4.1 EQUIVALENT WIDTHS AND CONTINUUM FLUX CORRELATIONS

Some results of the analyses of equivalent-width *versus* continuum flux correlations are given in Table 8. The four main conclusions from these and other correlation tests are as follows.

(i) *The equivalent widths of highly-ionized absorption lines are correlated with continuum flux, in the positive direction.* Those of the low-ion lines are well correlated with F_ν in the *negative* direction (for an example plot, see fig. 10 of Bromage *et al.* 1982). Intermediate ions such as C II, C III, Si III are rather poorly correlated with the continuum, and have approximately constant equivalent widths except at very-low-state epochs, when all W_λ are small.

(ii) *The absorption line equivalent widths are generally not correlated with the 'far ultraviolet excess' continuum.* All equivalent widths correlate better with the continuum F_ν at $\lambda 2500$ than with F_ν at $\lambda 1455$. This supports the two-component continuum model proposed in Paper I and

Table 8. Correlations of absorption-line equivalent widths (W_λ)(Å) with continuum flux levels F_ν(mJy).

Results of linear correlation tests (see Appendix) are given as:

R = linear correlation coefficient before allowance for errors

R' = linear correlation coefficient after error allowance (P = apparently perfect correlation)

m = slope of best-fit straight line (units are Å.mJy^{-1}) (L = value has low statistical significance since |R'-R| is large)

Absorption Feature (Å)	Dominant Contribution	I.P. (eV)	W_λ with F_ν(λ 2500) R(R')	m
2800	Mg II	8-15	-.13(P)	L
2600 +1610	Fe II	8-16	-.37(P)	L
1190	Si II	8-16	-.78(P)	-.2
1260	Si II	8-16	-.67(.69)	-.6
1530	Si II	8-16	-.58(P)	L
2945	He I	0-24	-.45(P)	L
1860	Aℓ III/II	6-28	-.54(.63)	-.4:
1370	?	?	-.32(.38)	
1335	C II	11-24	-.13(.16)	
1300	Si III	16-33	-.20(.22)	
1175	C III	24-48	-.32(P)	L
1394 +1402	Si IV	33-45	+.66(P)	+.5
1550	C IV	48-64	+.24(.44)	+.1:
1240	N V	77-97	+.88(.95)	+.3

developed in Papers II and III. The component that dominates at $\lambda 2500$ (the non-thermal power-law flux) appears to be closely associated with the source of ionizing photons that controls the ionization conditions in the absorption line region. At $\lambda 1455$ the power-law component is diluted by the second (possibly thermal – see Paper III) continuum component – the 'far ultraviolet excess'. The highly ionized absorbers are not even mildly correlated with this excess (as measured by its component $\Delta F_\nu^c(1455)$ defined in Paper II): for Si IV, $R=+0.2$; whilst for N V, $R=-0.2$.

(iii) *Excluding 'anomalous-continuum' epochs from the data set improves correlation of W_λ and F_ν ($\lambda 2500$).* This is particularly true of low ions like Si II, Mg II, C II. By 'anomalous-continuum' epochs are meant those when the far-ultraviolet excess component is very low and the continuum can be represented by a single power law across the whole *IUE* range. For example, the anomalous epoch Si II W_λ values are always systematically lower than the rest (see Fig. 4). This cannot be explained by enhanced ionization since Si III and IV are not particularly strong at anomalous epochs. Possible explanations involving transient optically thick sites of Si II absorption in the outer parts of the accretion disc or innermost parts of the BLR, seem to be ruled out on velocity grounds. There is therefore at present no satisfactory explanation of this effect.

(iv) *Low-ion absorption equivalent widths are directly proportional to one another,* that is, they are near-perfectly correlated ($R>0.75$, $R'>0.85$), and each best-fit line runs through the origin (within the errors). All the lines studied (1190, 1260, 1300, 1530, 1860 and the unidentified 1370) vary together in unison, even through the anomalous epochs. Furthermore, this result holds even though the individual relationships with F_ν are not truly linear.

4.2 MEAN WAVELENGTHS AND WAVELENGTH SHIFTS

Trends in effective wavelengths (Table 5) have been quantified by performing linear correlation tests on the W_λ *versus* $\Delta\lambda$ relationships (see Appendix B). The principal results are as follows:

(i) *The most reliable mean effective wavelengths (C II, Si IV and N V) yield mean velocities of $-820\,(\pm 100)$ km s^{-1} relative to the emission lines.* For lines other than C II, Si IV and N V, estimates of absolute velocities are rendered more uncertain because of blending of species or greater local-continuum curvature (for N V the effects of Lyα and N V emission wings tend to cancel out). Even for C II and N V, the relative contributions of the two lines in each feature are uncertain: if N V is optically thin, the mean effective velocity is -700 km s^{-1}, if in the optically thick limit, -850 km s^{-1}. The distorting effect of the Galactic contribution to the C II feature has been allowed for in this calculation, so that the mean of -820 km s^{-1} refers to the active nucleus of NGC 4151.

(ii) *Effective wavelengths for the high ions C IV, Si IV and N V are correlated with their W_λ values – when the lines strengthen they shift to slightly longer wavelengths.* The effect is particularly noticeable for the well-observed I1 flare event. The shifts amount to the equivalent of about 360 km s^{-1} for N V and 270 km s^{-1} for C IV. Only about half of this (at most) could arise from doublet-ratio (saturation) changes, so there appears to be evidence for real mean velocity shifts of order 150 km s^{-1}.

The shifts are towards less negative velocities when the continuum brightens. These shifts in mean velocity are therefore in the same sense and of the same order of magnitude as those seen in C IV velocity profiles from high-dispersion data (Table 6).*

*Note that variations in the C IV emission-line *V*/*R* ratio constitute a less reliable estimate of velocity shifts than suggested in Paper I. Now that the database is more representative of extreme cases, it is apparent that variations in *V*/*R* can also be caused by changes in the emission width. Furthermore, the apparently extreme change in *V*/*R* between 1978 February and later, is now believed due to incompleteness of ITF calibration tables during the 1978 February commissioning phase data reductions.

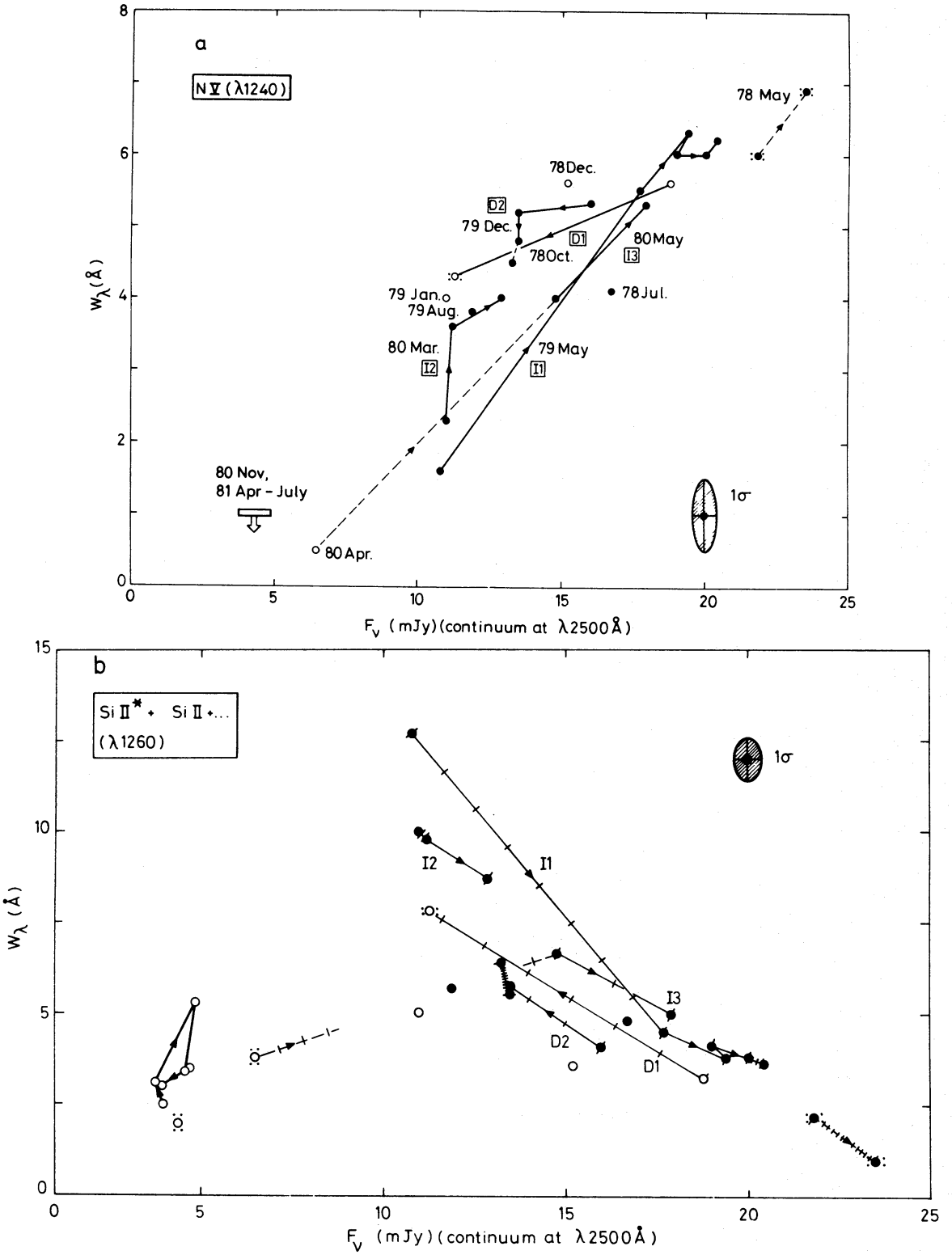

Figure 4. (a, b) Graphs of equivalent widths versus λ2500 continuum flux, for *all* epochs (1978–81) with points connected where epochs separated by less than about 2 weeks. The main events are labelled. Time lags between continuum changes and absorption line strength changes (see Section 7) would show here as loops, being anti-clockwise for positive correlations (a – N v) or clockwise for negative correlations (b – Si II λ1260). In (b) connections are marked off in intervals of 2 days where convenient. Colon signs indicate much larger than average errors (the average being indicated by the error ellipse).

There is no evidence here for time lags for N v, and only weak and conflicting evidence for Si II lags (see especially the I1 event line, compared with the clear C IV *emission* lags demonstrated in paper III).

'Anomalous continuum epochs' are marked with open circles: note that for Si II these points lie systematically low (see Section 4.1).

(iii) Any wavelength (velocity) shifts of low-ion absorption lines are difficult to disentangle because of line blending at low dispersion. However, for those ions least affected by blends and saturation uncertainties (C III, He I, Fe II) there are very weak anticorrelations of $\Delta\lambda$ with W_λ (that is, when these low ions strengthen, they shift to slightly shorter wavelengths). This would support result (ii) above if confirmed.

(iv) *The mean observed wavelengths (last row of Table 5) of the λ1300, 1260 and 1190 features clearly confirm that the excited levels of Si II* $3s^2 3p\ ^2P_{3/2}$ (0.04 eV) and Si III** $3s3p\ ^3P$ (6.6 eV) are well populated.* Even after allowance for an assumed mean velocity shift of $+140\ \mathrm{km\ s^{-1}}$ from λ_0 positions [derived from result (i) above], the mean observed λ1260 and λ1190 wavelengths are closest to the positions of the excited-level lines.

(v) Finally, the very high $\Delta\lambda$ for λ1860 can only partly be explained by optical thickness effects or blending of Al III with the Al II** lines. Since the velocity range (Table 7) is not unusual, there are only two possible explanations: either there is a strong (unidentifiable) extra line in the blend, or else the Al III lines fall coincidentally close to a small gap in a forest of weak emission lines. In either case the tabulated equivalent widths and wavelengths from the low-dispersion data must still be treated with caution.

5 Results: column densities for absorption region

In principle, ion column densities derived from the *IUE* absorption spectrum may be used to calculate a total N(H) value for the instantaneous line-of-sight through the absorption line region. This latter may then be compared with the very large hydrogen columns deduced from soft X-ray photoelectric absorption measurements for this active nucleus. Values of N(H) varying between 4×10^{22} and $2\times10^{23}\ \mathrm{cm^{-2}}$ have been derived from the X-ray data (Ives *et al.* 1976; Barr *et al.* 1977; Holt *et al.* 1980). Unfortunately, however, only a lower limit to gas columns can be derived from the ultraviolet absorption spectrum, because:

(i) not all ionization and excitation states are represented in the *IUE* spectra;

(ii) the detailed velocity structure is not well known, and hypothetical large columns with small b values can remain undetected when blended with broader components;

(iii) the geometrical arrangement and motions of absorbing clouds in the line-of-sight relative to the emission line region and continuum source are still poorly understood.

Elements represented best in the *IUE* spectra are C and Si. In each case, the neutral atoms are not detected, and fifth and higher stages of ionization are unobservable but may have significant populations. For carbon, C II, C II*, C III** and C IV are accessible to *IUE* but neither C II** nor (crucially) the C III ground state give rise to any lines within the *IUE* range. For silicon the situation is only slightly better: Si II, Si II*, Si II**, Si III** and Si IV are all measurable, but the important Si III λ1206 resonance line proves difficult since it is severely blended with strong broad Lyα absorption, and overlaid with Lyα geocoronal emission at low resolution.

Before we can go on to calculate total column densities, we must of course have some information on the velocity dispersions (line profiles) of the absorbers. Noting that the resolved Si IV doublet appears to be only partly saturated (doublet ratio is always more than 1; Table 4) we first consider single-Gaussian-shaped profiles and calculate N and the velocity dispersion parameter b at various epochs. This model is broadly consistent with the observed high-dispersion line profiles, widths and doublet strengths (Fig. 1, Table 6, Table 7; and also Penston *et al.* 1979, and Penston *et al.* in preparation, the latter for the Mg II doublet).

Consider the flare event I1. We have the following measurements using the HLC Si IV definition and the low-dispersion data (Tables 2 and 4):

$DR=1.8\pm0.1$ and $W_{1403}=2.5\pm0.5$ (pre-flare, May 3);

and

$DR=1.3\pm0.1$ and $W_{1403}=4.7\pm1.0$ (flare, May 21–31).

From these we obtain b values:

$b=570^{+180}_{-130}\,\mathrm{km\,s^{-1}}$ (pre-flare) and 470^{+350}_{-180} (flare),

These are the same, within the uncertainties. A value of $\sim500\,\mathrm{km\,s^{-1}}$ for b is also consistent with Si IV doublet observations at other epochs, including the well-observed 'intermediate state' epochs of 1979 December 12, 13 and 1980 January 1, although there is a very slight trend towards higher values of b at lower flux levels as with the I1 results. Unfortunately the C IV and N V resonance doublets are unresolved at low dispersion, but the small number of measurements of the Fe II $\lambda\lambda$ 2585, 2599 doublet (Table 3) also indicate a degree of saturation consistent with a b value of a few hundred $\mathrm{km\,s^{-1}}$.

Effective b values within the range determined above ($500^{+250}_{-150}\,\mathrm{km\,s^{-1}}$) are also obtained from consideration of the high-dispersion data for both high and low ions (Fig. 1; Tables 6, 7). Consider the N V lines in the mean 'high-state' spectrum (Table 7). The velocity range seen is from about -900 to $-300\,\mathrm{km\,s^{-1}}$ relative to the emission lines. Further, the mean velocity from low-dispersion data [Section 4.2, results (i) and (ii)] is about -650. The N V lines are then quite symmetric, with an effective velocity dispersion $\sim250\,\mathrm{km\,s^{-1}}$ and corresponding b value $\sim400\,\mathrm{km\,s^{-1}}$. Some other absorptions appear to be a little broader and more asymmetric, covering a wider velocity range -1100 to $+100$ around the effective mean of $\sim-650\,\mathrm{km\,s^{-1}}$. The observations are all consistent with b values in the range $500^{+250}_{-150}\,\mathrm{km\,s^{-1}}$, however, and this applies to both high and low-ionization species.

These results indicate that the NGC 4151 absorption line variations are due mainly to changes in the column density (N) of the species absorbing, rather than to changes in the b values for the assemblage of absorbing clouds.

Assuming an effective $b=500\,\mathrm{km\,s^{-1}}$ for all ions column densities for the various observed carbon and silicon ions have been calculated, using the equivalent widths listed in Table 4. For carbon ions we find:

$$N(\mathrm{C\,II+C\,III+C\,IV})=\begin{cases}[3.0+(>3.5)+1.3]\times10^{15}\,\mathrm{cm^{-2}}\ \text{(pre-flare)}\\ [2.4+(>1.7)+4.6]\times10^{15}\,\mathrm{cm^{-2}}\ \text{(flare)}\end{cases}$$

where a lower limit for C III assuming $N(\mathrm{C\,III})>5\times N(\mathrm{C\,III}^{**})$ is assumed, corresponding to the high-density limit for reasonable temperatures ($T_e\lesssim5\times10^4$). Hence, we have $N(\mathrm{C})>9\times10^{15}\,\mathrm{cm^{-2}}$. (If the b value were in fact not 500 but $250\,\mathrm{km\,s^{-1}}$, we would have $N(\mathrm{C})>8\times10^{16}\,\mathrm{cm^{-2}}$).

Similar arguments for silicon ions lead to:

$$N(\mathrm{Si\,II+III+IV})=\begin{cases}[5.5+(>5.4)+0.6]\times10^{15}\ \text{(pre-flare)}\\ [0.5+(>0.8)+2.0]\times10^{15}\ \text{(flare)}\end{cases}$$

so that for $b=500$, $N(\mathrm{Si})>1.2\times10^{16}\,\mathrm{cm^{-2}}$. (For $b=250$, this would be $>3\times10^{17}$.)

Making the further reasonable assumption of solar elemental abundances (*cf.* Barr *et al.* 1977, Holt *et al.* 1980) yields

$$N(\mathrm{H})\gtrsim10^{21}\,\mathrm{cm^{-2}}$$

where the inequality derives from the adoption of lower limits for C III and Si III, from the assumption of ultraviolet covering factor of unity and from ignoring any saturated cloud components with $b\lesssim50\,\mathrm{km\,s^{-1}}$. This lower limit for $N(\mathrm{H})$ can be compared with the $N(\mathrm{H})\sim10^{22}$–10^{23} derived from soft X-ray data.

6 Results: electron density in absorption region

Electron densities n_e, or limits on them, can be estimated from several separate aspects of the *IUE* data – from the relative strengths of excited fine structure lines, from considerations of metastable-level populations, and from observed ion recombination times (Anderson 1974).

6.1 EXCITED FINE STRUCTURE LINES

Absorption is present in the excited fine structure lines (EP 0.04 eV) of Si II at $\lambda\lambda$ 1265, 1309 and 1533. The corresponding ground state lines are blended in the first two cases with S II/Fe II and Si III/O I respectively, but λ 1526.70 is detectable on the wing of C IV and is free from blending. From the high-dispersion spectra, the excited line seems to be (in the high state) as strong as, and (1978 December 25) nearly twice as strong as, the resonance line. Absorption in the excited fine structure line (EP 0.01 eV) of C II is also presumably present but it is strongly blended with the resonance line. Excited levels (EP up to 0.12 eV) of Fe II multiplets 2 and 1 and perhaps others are also detected in some spectra (see Figs 1 and 2), whilst $\Delta\lambda$ values from low-dispersion spectra confirm the Si II* identifications.

There are several possible mechanisms for populating the excited $J=3/2$ level of Si^+. These are: (i) collisions with electrons, protons and hydrogen atoms; (ii) direct infrared excitation; (iii) ultraviolet pumping; and (iv) recombination.

At densities above $n_e \sim 5\times10^3\ \mathrm{cm}^{-3}$, collisions will dominate and set up a 2:1 ratio in accordance with the statistical weights. It seems quite probable from the discussion in the next sections that the density in the absorbing cloud is actually much higher than this. It is therefore to be expected that statistical equilibrium is established and the excited fine structure lines should indeed be stronger (by a factor 2 in the optically thin case), consistent with the observations. No determination can be made in this case of the effects of infrared or ultraviolet pumping discussed by Bahcall (1967) for quasars.

6.2 ABSORPTION LINES FROM MESTASTABLE STATES

Several absorption lines in NGC 4151 spectra arise from metastable states. These include the Balmer lines and He I λ 3889 seen in the optical (Anderson & Kraft 1969), C III λ 1176, Si III λ 1297, He I λ 3188, 2945, 2829, 2764, and possibly He II λ 1640 and lines of Si II and Al II (see Table 3 and Figs 1 and 2). Probably the easiest case to consider here is that of C III, since the observed absorption is unblended and the relevant atomic physics is well studied.

In principle, the same excitation mechanisms apply to these C III $2s2p\ ^3P$ metastable levels as were listed in the last section. However, only collisions from the ground $2s^2\ ^1S$ and dielectronic and radiative recombination need be considered, since radiative processes via discrete levels between the initial (ground) and final (metastable) terms must involve at least one slow (intersystem or forbidden) transition. Processes depopulating the metastable levels of $2s2p\ ^3P^0$ include radiative decay via λ 1909, collisional excitation and de-excitation and photoionization. Thus the population balance equation becomes:

$$n_{\mathrm{III}^{**}}\left(A+n_e q^{\mathrm{D}}+n_e\sum_j q_j^{\mathrm{E}}+\int_{\nu_0}^{\infty}\frac{\pi F_\nu}{h\nu}\alpha_P\,d\nu\right)=\alpha_{\mathrm{R}}n_e n_{\mathrm{IV}}+q^{\mathrm{E}}n_e n_{\mathrm{III}}$$

where

$n_{\mathrm{III}^{**}}$	is the space density of twice ionized ions in the metastable levels,
n_e	is the electron density,
n_{III}, n_{IV}	are the densities of (ground state) twice and three times ionized ions, respectively,

A is the radiative decay rate from the metastable level,
$n_e q^E$, $n_e q^D$ are the collisional excitation and de-excitation rates, respectively,
F_ν is the ionizing flux at frequency ν,
ν_0 is the threshold frequency for ionizing from the metastable level,
α_P is the cross-section for photoionization from the metastable level and
α_R is the effective coefficient for recombination to the matastable level.

To estimate F_ν in the photoionization term is rather difficult since the distance of the absorbing cloud from the nucleus, and the ionizing spectrum at the relevant frequencies, are unknown. Therefore, it seems most general to write

$$An_{\text{III}^{**}}+\left(q^D+\sum_j q_j^E\right)n_e n_{\text{III}^{**}}<\alpha_R n_e n_{\text{IV}}+q^E n_e n_{\text{III}}. \tag{3}$$

Inserting numerical values from Dufton *et al.* (1978), Nussbaumer & Storey (1978) and Storey (1981) for a temperature of $T_e=2\times10^4$ K, which is appropriate to conventional photoionization-equilibrium models for broad line regions of active galactic nuclei (see e.g. Davidson 1972), we have:

$$\frac{n_{\text{III}^{**}}}{n_{\text{IV}}}<\frac{2\times10^{-4}+0.2(n_{\text{III}}/n_{\text{IV}})}{1+5\times10^9 n_e^{-1}}. \tag{4}$$

(Here it has been assumed that the individual $2s2p\ ^3P$ levels are in statistical equilibrium. Collisional excitation from ^3P to $2p^2\ ^1P$ and ^1D has been included.) We note also that the highest value of $n_{\text{III}^{**}}/n_{\text{III}}$ is ~0.2, for thermal equilibrium (Boltzmann factor).

Now, using the absorption lines λ1176 and λ1550, an observed value can be estimated for the ratio of the *column* densities (capital N's) of C III** and C IV. The transition probabilities of Nussbaumer & Storey (1978) lead to $\Sigma f_{abs}=1.37$ for the λ1176 multiplet, and a weighted mean $\lambda_{abs}=1175.94$ Å. The equivalent width of λ1176 is usually 3±1 Å but reached 4.5±1 Å in the pre-flare state. Thus,

$$N_{\text{III}^{**}}>\begin{cases}2.7\pm0.6\times10^{14}\,\text{cm}^{-2}\ \text{(pre-flare)}\\ 1.8\pm0.6\times10^{14}\,\text{cm}^{-2}\ \text{(generally)}\end{cases}$$

assuming unsaturated lines to compute these lower limits. Combining the same measurements with the columns of C IV derived in Section 5 and assuming $b=500\,\text{km s}^{-1}$ for both species yields:

$$\frac{N_{\text{III}^{**}}}{N_{\text{IV}}}=\begin{cases}40(\pm^{20}_{15})\times10^{-2}\ \text{(pre-flare)}\\ 6(^{+7}_{-4})\times10^{-2}\ \text{(flare)}.\end{cases} \tag{5}$$

Values of the *space* density ratio as high as this certainly cannot be attained via recombination alone; the maximum ratio would be about 3×10^{-4}. Therefore, the main populating mechanism for the metastable levels must be assumed to be collisional, and there must be a substantial column of C III in its ground state. Unfortunately, the latter cannot be measured at present since the resonance line λ977 will remain inaccessible until the next generation of ultraviolet satellites. Little direct progress can be made with the analogous Si III problem either, because the Si III λ1206 resonance is severely blended with Lyα broad absorption and overlaid with geocoronal Lyα emission, in the *IUE* spectra.

If a 'single-point' model is approximately valid so that the observed column density ratio also applies approximately to mean space densities, then we can combine (4) and (5) to derive a relationship between $(N_{\text{III}}/N_{\text{IV}})$ and n_e. Consider the pre-flare observations. Even at the highest densities in the emitting BLR (10^{10}–$10^{11}\,\text{cm}^{-3}$) we would have $N_{\text{III}^{**}}/N_{\text{III}}\lesssim0.2$, whilst

$N_{III^{**}}/N_{IV}\sim 0.4$, and hence $N_{III}/N_{IV}\gtrsim 2$. At the lower densities $n_e = 10^9, 10^8, 10^7$, (N_{III}/N_{IV}) would be greater than about 10, 100, 1000, respectively, where the inequality derives from neglecting depopulation of III** by photoionization to IV. (Note also that if the assumed temperature were halved to only 10^4 K, these ratios would be even higher, by a factor of six or so.) Now, the limited observational evidence on Si III λ 1206 absorption (*cf.* Fig. 2), together with the assumption that $N(H) < 10^{23}$ (*cf.* Section 5) leads to the expectation that $(N_{III}/N_{IV}) \lesssim 30$ and hence $n_e \gtrsim 10^{8.5}$.

Similar analyses to the above are (in principle) possible for other observed metastable levels (Si III, Al II, Si II, etc.), although these are difficult to disentangle from blended resonance lines, and at present many of the relevant atomic data are less well known. Population mechanisms for the metastable levels of He I, H I and He II, are likely to be different, namely, recombination in the first case (Ives *et al.* 1976) and resonance self-absorption in H I and He II (Netzer 1975).

6.3 DENSITIES FROM RECOMBINATION TIMES

Anderson (1974) derived a lower limit to the absorption line region density, $n_e \gtrsim 5\times 10^6\,\mathrm{cm}^{-3}$, from the observations that the Balmer metastable absorptions were varying on the time-scale of 15 days or less. With the present coverage of flares in the ultraviolet, it is now possible to apply the same arguments on recombination times to estimate n_e limits from other lines. The ions that have shown the most dramatic changes in the *IUE* spectra are N^{4+} and Si^+.

Consider the N V changes with time, illustrated in Fig. 3. First, note that from 1980 March 6 to April 21, the N^{4+} had all but completely recombined. From this observation and the recombination coefficients of Aldrovandi & Péquignot (1973) for $T_e \simeq 2\times 10^4$, $n_e \gg 10^{4.5}\,\mathrm{cm}^{-3}$. A tighter limit derives from the 1978 October event (D1). Between the high-resolution observation of October 23.9 and the low-resolution observations of October 31.98, the N V incompletely recombined, giving $n_e \gtrsim 10^{5.2}$. The changes in Si^+ during the I1 event also imply $n_e > 10^5$. Finally, the apparently fast change in Si IV strength in one day in 1979 (May 3–4) unfortunately relies on a single noisy spectrum for the May 4 epoch, but if confirmed such a fast change would imply $n_e \gtrsim 10^6$.

The limits on n_e from recombination-time arguments are thus certainly consistent with the best estimates from metastable absorption line considerations (Section 6.2).

7 Discussion

Now we draw together the main conclusions from the ultraviolet absorption spectrum and its variations, and discuss their implications for models of the absorption-line region – its structure, density, ionization conditions, location and size.

Discussions of the nature and structure of the absorption region follow early papers by Anderson & Kraft (1969), Cromwell & Weymann (1970) and Anderson (1974), who considered both spherical-shell and discrete-cloud models. The more recent X-ray data (Barr *et al.* 1977; Holt *et al.* 1980) have been interpreted by Holt *et al.* (1980) as evidence that the photoelectric absorption of the soft X-rays occurs in a number (~100) of relatively small BLR clouds covering the source along our line-of-sight, with an average thickness of about two clouds, each of them being very thick ($\gtrsim 10^{22}\,\mathrm{cm}^{-2}$). Ferland & Mushotzky (1982) further suggest that these saturated absorption clouds, characterized by thermal linewidths ($\sim 10\,\mathrm{km\,s}^{-1}$) and large relative motions ($\sim 10^3\,\mathrm{km\,s}^{-1}$), are also *fully* responsible for the ultraviolet absorption lines. In their model, the absorbers may also only cover the continuum source and not the BLR emission line clouds.

The conclusions drawn from our new UV observations conflict with the Ferland & Mushotzky BLR model. The Si IV doublet ratios clearly indicate much thinner clouds in the absorption region. In addition the velocity range and structure is essentially the same for the wide range of

observed ion stages and is consistent with the total Si IV doublet ratios – suggesting an effectively smooth velocity dispersion ($b \sim 500\,\mathrm{km\,s^{-1}}$) in an overall bulk outflow of $\sim 700\,\mathrm{km\,s^{-1}}$.

Instead of the Ferland & Mushotzky (1982) picture, the ultraviolet data suggest either (i) a rather smooth, accelerating or decelerating outflow (wind); or (ii) a shell containing a very large number ($\gtrsim 10^8$?) of optically thin clouds with small thermal motions but $\sim 500\,\mathrm{km\,s^{-1}}$ dispersion amongst the cloud velocities, and with their velocity dependent on density or distance from the nucleus. From this, it is not surprising that there are large discrepancies between the column densities predicted by Ferland & Mushotzky and those derived by us. Notably, the total gas column density $N(\mathrm{H})$ now derived from the ultraviolet lines (Section 5) is $N(\mathrm{H}) \gtrsim 10^{21}\,\mathrm{cm^{-2}}$, to be compared with the soft X-ray absorbing column of $\sim 10^{22-23}\,\mathrm{cm^{-2}}$. The relationship between these two estimates remains an open question, which will hopefully become clear from simultaneous X-ray and ultraviolet spectral observations, such as we are undertaking with *EXOSAT* and *IUE*.

The correlations between absorption line velocities and continuum brightness (Section 4.2), interpreted in the pictures (i) and (ii) mentioned above, probably reflect the fact that material of the correct ionization state to produce those absorptions is at different positions in the flow of material at different times. However, because of the well-known problem of the ionization parameter (U) being spatially constant if $n \sim r^{-2}$ (Davidson & Netzer 1979), it is still difficult to decide whether the observations imply a run of velocity increasing outwards (accelerating flow) or inwards (decelerating flow). The choice is critically dependent on the adopted form of the $n(r)$ function, which is of course not well known.

The close correlations of absorption equivalent widths with continuum flux (Section 4.1) coupled with the wide range of ionization stages observed further strengthen the argument that photoionization by the non-thermal photons governs the ionization balance of the ultraviolet and optical absorbers.

The non-thermal photoionization conditions in the absorption region can be judged from the correlation trends with ionization potential (Table 8). They strongly suggest that the dominant ionization state in the absorption region is (in the case of carbon and silicon for example) doubly ionized. This leads to a value for the ionization parameter: $\log U \sim -2.5$ (Ferland & Mushotzky 1982; Ferland & Netzer 1983).

The presence of absorption lines from metastable levels leads to estimates of minimum space densities: $n_e \gtrsim 10^{8.5}\,\mathrm{cm^{-3}}$ (Section 6.2). Now, an upper limit on n_e of 10^{10} would be set if the absorption region were identified with that part of the BLR that emits C III]: we argue later that this region does indeed include the absorption region. In Paper III we concluded that the *inner* parts of the BLR have $10^{10} \lesssim n_e \lesssim 2\times 10^{10}\,\mathrm{cm^{-3}}$. Since it seems probable that density decreases outwards through the BLR, our best estimate for the absorption region density is in the range $10^{8.5} \lesssim n_e \lesssim 10^{10}$. Combining this density with the value of U gives the position of the absorption region to be about $R \simeq 10^{17.7\pm 0.4}\,\mathrm{cm}$.

We recall that our investigation of the strong emission lines (Paper III) presented evidence for stratification in the BLR. Three 'layers' were distinguished and labelled respectively BLR1, BLR2 and BLR3. The innermost layer BLR1 has a radius $R \sim 3\times 10^{16}\,\mathrm{cm}$ and velocities $V \sim 10-16\times 10^3\,\mathrm{km\,s^{-1}}$. Subregion BLR2 has $R \sim 6\times 10^{16}$, $V \sim 6-10\times 10^3$, and $n_e \gtrsim 10^{10}\,\mathrm{cm^{-3}}$. Finally BLR3 has $R \sim 10^{18}$, $V \lesssim 6\times 10^3$ and $n_e \lesssim 10^{10}$. The position of the absorbing region relative to BLR1, BLR2 and BLR3, is obviously of considerable interest.

Regions covered by absorbers include both continuum source and some or most of the BLR emission: both BLR1 and BLR2 are absorbed (see Figs 1 and 2 and Penston *et al.* 1979). Furthermore, the very low state (1981 May) C IV data indicate that both continuum and some (~20 per cent) BLR3 were absorbed then. (At these epochs, neither BLR1 nor BLR2 were radiating C IV.) Positioning the absorbers in BLR3 near $R \sim 3\times 10^{17}$ or beyond thus gives

consistency with both observed coverage of emission velocities and the most likely n_e and U values (see above). However, note that the range of absorption velocities is far less than the total range of emission: judged as a P Cyg profile, the lines are of Beals Type III (Beals 1951).

The lack of any clear evidence for time lags between continuum flares and absorption equivalent widths (see Figs 3 and 4 and the caption to Fig. 4) is significant here. Any time lags between 3 and 30 days should be detectable in the data. The radii of BLR1 and BLR2 are estimated to be about 10 and 20 light days, respectively (see Paper III). Thus, if the absorbers were in BLR1 or BLR2, the spread in time between the light travel time for the centre of the absorption region and that for the limb, would be of this order. This would lead to detectable mean time lags between continuum flares or decays and the absorbers' response to them (*cf.* observed C IV broad emission time lags reported in Paper III). There is no clear evidence for any such lags in Figs 3 and 4, suggesting that the absorption region is probably well clear of BLR1 and 2. A value of $R \sim 3\times10^{17}$ or beyond, is again indicated.

Consider now the likely thickness, ΔR, of the absorption region if it is a spherical shell. We have that $\Delta R \simeq N(\mathrm{H})/n_e$, with $10^{21} \lesssim N(\mathrm{H}) \lesssim 10^{23}$, and $10^{8.5} \lesssim n_e \lesssim 10^{10}$. Hence, $10^{11} \lesssim \Delta R \lesssim 10^{14.5}$. Furthermore, since $R \gtrsim 10^{17}$ in order to be clear of BLR2, we must have $(\Delta R/R) < 1$ per cent, with a best estimate of $(\Delta R/R) \sim 0.01$ per cent.

Such a shell at $R \sim 3\times10^{17}$ cm cannot completely cover the NGC 4151 BLR regions or it would emit more than 4×10^{-12} erg cm^{-2} s^{-1} in Hβ and outshine the whole of BLR3 Hβ emission which is observed to be 1.8×10^{-12} (Osterbrock & Koski 1976). This limits the covering factor of the absorption region to $f \lesssim 0.1$.

Assuming $N(\mathrm{H}) = 10^{22}$ cm^{-2} and $R^2 f = 10^{34}$ cm^2, the total mass in the BAL region is $\sim 1\, M_\odot$. The mass loss rate depends on whether it is assumed to be steady or episodic (Cromwell & Weymann 1970). If we assume that the shell or assembly of clouds is *not* being continually fed by material that goes undetected until it enters the shell at $R = 10^{17.5}$ cm, then the mass loss rate for the nucleus is only $\sim 10^{-2}\, M_\odot$ yr^{-1} or less. This shrinkage of the original 'cornucopia of matter' announced by Anderson & Kraft (1969) is fortuitously similar in scale to the reduction proposed by Cromwell & Weymann (1970), who first introduced the episodic picture.

This paper has provided detailed identification and correlation studies of the NGC 4151 absorption line spectrum. The analyses have yielded better estimates of the absorbing region location, size, structure and density than hitherto. Yet there are of course still many unsolved problems requiring observers' attention.

The sampled flares I1 and I3 were invaluable to this analysis, but for example the important transition from very low quiescent state to the pre-flare condition has not yet been monitored. A detailed sampling at $\lesssim$4-day intervals in X-rays *and* ultraviolet of any large flare would be crucial material for further modelling of the response of the various nebular sub-regions. The long-standing problem of the relationships between soft X-ray and UV–optical gas columns N(H) and their respective locations can only be solved by simultaneous observations (with *IUE* and *EXOSAT* initially). Higher velocity resolutions and better signal-to-noise ratios – such as should be attainable with the *Space Telescope*– are needed in order to look for fine velocity structure, saturated clouds, and the separation of Galactic halo and interstellar absorptions from the NGC 4151 nuclear ones.

Complementary studies of BAL quasars (Weymann & Foltz 1983) and other absorption-line Seyferts are also needed, to see if they vary in similar ways to NGC 4151, and to study these phenomena over a wide range of luminosities of Active Galactic Nuclei.

Acknowledgments

We are grateful to the ESA and SERC *IUE* selection committees for generously supporting the observational programme. We would like to thank Dr Prab Gondhalekar of Rutherford

Appleton Laboratory for his help with the observing campaigns. GCP acknowledges financial support from the Italian CNR and MPI.

References

Aldrovandi, S. M. V. & Péquignot, D., 1973. *Astr. Astrophys.*, **25,** 137.
Anderson, K. S., 1974. *Astrophys. J.*, **189,** 195.
Anderson, K. S. & Kraft, R. P., 1969. *Astrophys. J.*, **158,** 859.
Bahcall, J. N., 1967. *Astrophys. J.*, **149,** L7.
Barr, P., Ives, J. C., Sanford, P. W. & White, N. E., 1977. *Mon. Not. R. astr. Soc.*, **181,** 43P.
Beals, C. B., 1951. *Publs Dom. astr. Obs.*, **9,** 1.
Boksenberg, A., Snijders, M. A. J., Wilson, R., Benvenuti, P., Clavel, J., Macchetto, F., Penston, M. V., Boggess, A., Gull, T. R., Gondhalekar, P., Lane, A. L., Turnrose, B., Wu, C. C., Burton, W. M., Smith, A., Bertola, F., Cappaccioli, M., Elvius, A. M., Fosbury, R., Tarenghi, M., Ulrich, M. H., Hackney, R. L., Jordan, C., Perola, G. C., Roeder, R. C. & Schmidt, M., 1978. *Nature,* **275,** 404.
Bromage, G. E., Boksenberg, A., Clavel, J., Elvius, A., Penston, M. V., Perola, G. C., Pettini, M., Snijders, M. A. J., Tanzi, E. G., Tarenghi, M. & Ulrich, M. H., 1982. *ESA SP-176*, p. 533.
Cromwell, R. & Weymann, R., 1970. *Astrophys. J.*, **159,** L147.
Davidsen, A. F. & Hartig, G. F., 1978. *Proc. COSPAR/IAU Symp. on X-ray Astronomy*, p. 377, eds Baity, W. A. & Peterson, L. E., Pergamon Press, Oxford.
Davidson, K., 1972. *Astrophys. J.*, **171,** 213.
Davidson, K. & Netzer, H., 1979. *Rev. Mod. Phys.*, **51,** 715.
Dufton, P. L., Berrington, K. A., Burke, P. G. & Kingston, A. E., 1978. *Astr. Astrophys.*, **62,** 111.
Ferland, G. J. & Mushotzky, R. F., 1982. *Astrophys. J.*, **262,** 564.
Ferland, G. J. & Netzer, H., 1983. *Astrophys. J.*, **264,** 105.
Gill, T. R., Lloyd, C., Penston, M. V. & Snijders, M. A. J., 1984. *Mon. Not. R. astr. Soc.*, **211,** 31.
Holm, A., 1979. *IUE–NASA Newsletter,* **7,** 27.
Holt, S. A., Mushotsky, R. F., Becker, R. H., Boldt, E. A., Serlemitsos, P. J., Szymkowiak, A. E. & White, N. E., 1980. *Astrophys. J.*, **241,** L13.
Ives, J. C., Sanford, P. W. & Penston, M. V., 1976. *Astrophys. J.*, **207,** L159.
Netzer, H., 1975. *Mon. Not. R. astr. Soc.*, **171,** 395.
Nussbaumber, H. & Storey, P. J., 1978. *Astr. Astrophys.*, **64,** 139.
Osterbrock, D. E. & Koski, A. T., 1976. *Mon. Not. R. astr. Soc.*, **176,** 61P.
Penston, M. V., Clavel, J. C., Snijders, M. A. J., Boksenberg, A. & Fosbury, R. A. E., 1979. *Mon. Not. R. astr. Soc.*, **189,** 45P.
Penston, M. V., Boksenberg, A., Bromage, G. E., Clavel, J., Elvius, A., Gondhalekar, P. M., Jordan, C., Lind, J., Lindegren, L., Perola, G. C., Pettini, M., Snijders, M. A. J., Tanzi, E. G., Tarenghi, M. & Ulrich, M. H., 1981. *Mon. Not. R. astr. Soc.*, **196,** 857 (Paper I).
Perola, G. C., Boksenberg, A., Bromage, G. E., Clavel, J., Elvis, M., Elvius, A., Gondhalekar, P. M., Lind, J., Lloyd, C., Penston, M. V., Pettini, M., Snijders, M. A. J., Tanzi, E. G., Tarenghi, M., Ulrich, M. H. & Warwick, R. S., 1982. *Mon. Not. R. astr. Soc.*, **200,** 293 (Paper II).
Storey, P. J., 1981. *Mon. Not. R. astr. Soc.*, **195,** 27P.
Ulrich, M. H. *et al.*, 1980. *Mon. Not. R. astr. Soc.*, **192,** 561.
Ulrich, M. H., Boksenberg, A., Bromage, G. E., Clavel, J., Elvius, A., Penston, M. V., Perola, G. C., Pettini, M., Snijders, M. A. J., Tanzi, E. G. & Tarenghi, M., 1984. *Mon. Not. R. astr. Soc.*, **206,** 221 (Paper III).
Weymann, R. J. & Foltz, C. B., 1983. In: *Quasars and Gravitational Lenses, Proc. 24th Liège Astrophysical Colloquium,* p. 538.

Appendix A: estimation of errors on low-dispersion measurements

Lines with widely different strengths and signal-to-noise ratios need to be compared quantitatively in order to extract the most information about the absorption line region and its response to the flaring continuum source. Thus, errors have to be individually estimated for each feature at every epoch. Errors on all the W_λ are given in Table 4. For simplicity, only *average* error values for $\Delta\lambda$ are presented in Table 5, with a colon indicating an error about twice the average, whilst the numbers of spectra per camera per epoch vary from 1 to 6 (see Table 1 of Paper II) and this affects accuracies in an obvious way.

In nearly all low-dispersion spectra, particle event 'spikes' were very rare, due to the short exposures involved. For this and other reasons, internal errors – that is, errors *within* the adopted definitions of lines – are expected to be almost random. They are assumed below to have normal error distributions, and standard errors are quoted in Table 4 for example. External errors for comparisons with other workers' future measurements are much more difficult to assess. They are relatively large when an absorption is superimposed on an emission line (e.g. C IV and Si II λ1530 in the C IV emission) but rather small and of the same order as the purely internal errors for cases like Si II λ1260 and C II λ1335 where the local continuum behaviour is clearer.

The internal errors derive from two sources: the uncertainty of the adopted continuum, F_c *within* its definition due to noise in the continuum windows, and the photometric errors on samples in the integration region itself. Quoted errors in Table 4 are the sum of two contributions, therefore. The first dominates for the wider, shallower features or where only very narrow continuum windows are feasible. This contribution has been calculated by directly following the error propagation from F_c, through to W_λ. The second contribution was taken to be given by $N^{-1/2}(aD^{1/2}M^{1/2}+bW_\lambda)$, where N is the number of spectra averaged; D is the continuum *IUE* DN count and M the number of sampling bins for the features; and a and b are camera-dependent parameters. Using test measurements on individual spectra within one epoch, values of a=0.01 (for SWP) and 0.02 (LWR), and b=0.04 were adopted here.

These definitions of errors are sufficiently representative, for example, to enable weak (or noisy) lines to be properly included in linear correlation tests against continuum changes and other quantities (see Section 4).

Errors on $\Delta\lambda$ have been derived in a corresponding way and are also used in correlation analyses in this paper. Note that in addition to these errors, the absolute λ scale adopted is subject to small systematic errors, which may amount to 1 Å for λ<2000 Å and perhaps 2–3 Å for λ>2000 Å (see Paper I). Such λ-scale errors are essentially the same for many lines (e.g. $\lambda\lambda$1200–1600) and independent of epoch and continuum flux. They are therefore ignored in the correlation studies presented here, and do not affect any of the conclusions drawn in Section 4.

Errors on continuum flux values, and values of the fluxes F_ν at λ1455 and λ2500 themselves, are taken from Table 3 of Paper II for the period up to 1980 May. For subsequent epochs, the continuum values have been newly derived here and are given in Table 4(c); the methods of Paper II were followed exactly.

Appendix B: Linear correlation analyses

The linear correlation analyses referred to in Section 4, were performed as follows. First, the linear correlation coefficient is defined as usual with no allowance for errors:

$$R=\frac{[x,\ y]}{\sigma_y\sigma_x} \tag{A1}$$

where σ_x^2, σ_y^2 and $[x, y]$ are the variance of x, variance of y and covariance of x and y, respectively. To allow for computed observational standard errors (such as those listed in Table 4) and hence derive a corrected correlation coefficient R' and best-fit straight line under the maximum likelihood principle, one calculates values of variances $\sigma_{\varepsilon,x}^2$ and $\sigma_{\varepsilon,y}^2$ for the total scatter variables ε_x and ε_y. If one assumes the mean absolute values of ε_x and ε_y are both zero, and $\sigma_{\varepsilon,x}^2$ and $\sigma_{\varepsilon,y}^2$ can be represented by the *mean-square* values of the observational standard errors on x and y respectively, then

$$R'=\frac{[x, y]}{[(\sigma_{y,y}^2-\sigma_{\varepsilon,y}^2)(\sigma_x^2-\sigma_{\varepsilon,x}^2)]^{1/2}} \tag{A2}$$

and the 'best straight-line fit' slope is given by

$$m=\left(\frac{\sigma_y^2-\sigma_{\varepsilon,y}^2}{\sigma_x^2-\sigma_{\varepsilon,x}^2}\right)^{1/2} \tag{A3}$$

For the present study R and R' have been calculated, together with slopes of the three straight-line fits [two least-squares solutions and equation (A3)], for testing the linear correlations between W_λ and continuum F_ν, and between $\Delta\lambda$ and W_λ.

Values of R, R' and m (equations A1, A2, A3) for the $\Delta\lambda$ versus W_λ relationship were calculated for two sets of data. First, only those epochs with more than two spectra and good signal-to-noise, between 1979 May 3 and 1980 January 1, were included, except that 1979 May 4 is also included to add to the crucial pre-flare May 3 representation. This is the most reliable set of data and covers the large flare event I1 and its following plateau of high flux levels, together with intermediate-state epochs in December–January. Secondly, data on all available epochs were used to assess correlations over the longer time-scale. There are several lines which are strongly correlated in $\Delta\lambda$ and W_λ over the restricted period 1979 May 3–1980 January 1. They are generally less well correlated when all epochs are added. The change in R may be simply because of the increased numbers of noisy data, but the corrected value R' should not show such an effect. A sharp drop in R' for example in Si II λ 1260 between the restricted and general data sets must be real.

For the equivalent width *versus* continuum flux F_ν relationships, correlation coefficients R and R' and best-fit slope m have been calculated for four data samples: (i) W_λ with F_ν (λ 1455) for the selected period 1979 May 3–1980 January 1 including I1 epochs with accurate data but dominated by the single event I1; (ii) W_λ with F_ν (λ 1455) for all the main monitored period, 1978 February–1980 May, including up to 31 epochs; (iii) W_λ with F_ν (2500) for all the same monitored period, including up to 24 epochs and (iv) W_λ with the λ 1455 component of the far-ultraviolet excess, $\Delta F_\nu^c(1455)$ as defined in Paper II. The main results are described in the text. The set (iii) is less extensive than (ii) because at 7 epochs no long-wave spectra were obtained. To test whether differences between (ii) and (iii) correlations might be distorted by the slightly different data sets, extra calculations were performed for the same 24 epochs as in (iii) but for W_λ *versus* F_ν (λ 1455). No important distortions were found, mainly because the additional epochs were essentially already represented in the basic 24 – no large 'events' were peculiar to the extra epochs. For both N V and Si II, for example, it was evident that differences between (ii) and (iii) correlations were real and highly significant. Intercombinations of W_λ were also investigated. The correlations of low-ion equivalent widths amongst themselves are particularly striking.

Copies of the full set of correlation plots produced in these analyses are available on request. Examples are shown in figs 3 and 10 of Bromage *et al.* (1982).